fibers

MDPI

Article

Chopped Basalt Fibers Reinforced Mortar for Strengthening the Architectural Heritage

Micaela Mercuri [1,*], Marco Vailati [2] and Amedeo Gregori [2]

[1] Department of Civil and Environmental Engineering, Northwestern University, Evanston, IL 60208, USA
[2] Department of Civil, Building-Architecture and Environmental Engineering, 67100 L'Aquila, Italy
* Correspondence: micaelamercuri2029@u.northwestern.edu

Abstract: The high seismic vulnerability of unreinforced masonry buildings urgently calls for researchers to develop sustainable reinforcing methods and materials. This paper presents an innovative lime-based mortar reinforced with randomly oriented basalt fibers for the reinforcement of masonry heritage. The main aim of this study is to understand the effect of the content and the length of basalt fibers on the mortar's mechanical behavior. As a cementitious material made mostly out of lime, the mortar is chemically compatible with the historical substrate and therefore suitable in cases of restoration works on architectural heritage. Moreover, the chopped basalt fibers are randomly oriented, and this characteristic makes the overall layer effective in all directions, as the state of stress induced by seismic action is directionally undetermined. The newly proposed reinforcement system is characterized by a twofold aspect related to sustainability: 30% of the aggregates composing the mortar mix design is a recycled result of the ruins of the 2009 L'Aquila earthquake, and the chopped fibers are made out of basalt, widely known for its environmentally supportable peculiarity. The study consists of testing samples characterized by two fiber lengths and six fiber contents, along with one set of plain mortar samples. Specimens measuring 160 mm × 40 mm × 40 mm are first tested in a three-point bending (TPB) configuration, aiming to determine the flexural strength and the post-peak capacity through the calculation of the fracture energy. Then, the two broken pieces resulting from the TPB tests, each measuring 80 mm × 40 mm × 40 mm, are tested in splitting and compression, respectively, aiming to compute the tensile and compressive strengths. Finally, to provide a trend for the mortar's mechanical properties, a regression analysis is performed by fitting the experimental data with simple linear, polynomial, and exponential regression models. Results show that: (i) both fiber content and fiber length are responsible for a linear increase of the flexural strength and the fracture energy; (ii) for both short- and long-fiber mortar samples, the tensile strength and the compressive strength parabolically increase with the fiber content; (iii) the increase in fiber content and fiber length always generates a reduction in the conglomerate workability. The fiber content (FC) optimization with respect to the mechanical properties leads to a basalt FC equal to 1.2% for long-fiber samples and an FC equal to 1.9% for short-fiber ones.

Keywords: vulnerability unreinforced masonry; strengthening systems; basalt chopped fibers; lime-based mortar; experimental campaign; analytical formulation

Academic Editors: Francesco Bencardino, Luciano Ombres and Pietro Mazzuca

Received: 29 November 2024
Revised: 10 January 2025
Accepted: 5 February 2025
Published: 11 February 2025

Citation: Mercuri, M.; Vailati, M.; Gregori, A. Chopped Basalt Fibers Reinforced Mortar for Strengthening the Architectural Heritage. *Fibers* **2025**, *13*, 20. https://doi.org/10.3390/fib13020020

1. Introduction

Structures made out of unreinforced masonry are very vulnerable to earthquakes [1–6], and their seismic susceptibility augments as structural size increases [7,8]. While developing new materials and seismic strengthening technologies for masonry architectural

heritage structures [9], there are several conservation principles to be considered [10–17], including concepts like compatibility and reversibility of repair, minimal intervention, monitorability, structural authenticity, and reliability. Italian codes progressively incorporated these concepts. In particular, first the 2011 Italian Guidelines [18] made an exhaustive list of principles to be observed during the design and execution of restoration works on cultural heritage. Then, the latest version of the Italian building code [19,20] prescribes the adoption of the Italian Guidelines, therefore implying the respect of the aforementioned principles.

Two are the traditional strengthening interventions on existing masonries: the fiber-reinforced polymers (FRP) [21–28] and composites made out of fiber-reinforced cementitious matrix (FRCM) [29–39]. FRPs demonstrated their effectiveness in increasing the load-carrying capacity of masonry elements [40,41], but they are characterized by several drawbacks, such as low fire resistance and permeability. They are not suitable for application on moistened walls and, most importantly, they have a deficient chemical affinity with the historical substrate made out of masonry [42,43]. The alternative use of FRCMs is advantageous because they are easy to place and install, and they have good vapor permeability [44]. FRCMs are generally composed of fiber fabrics embedded in a matrix, which is most often a cement-based mortar [45–50]. Many are the materials used for the fibrous component, i.e., steel [51,52], carbon [53,54], glass [55,56], aramid [57,58], and polyvinyl-alcohol (PVA) [59]. During the last few decades, vegetable fibers have shown to be a valid alternative as a fibrous matrix in composite materials [60–63]. It is undeniable that FRCM is an advantageous technique for strengthening masonry structures, but it is, however, characterized by many drawbacks for interventions on historical heritage. For example, the most widely adopted mortar matrix for FRCM is mostly composed of cement, which does not ensure chemical compatibility with the existing substrate. Moreover, the FRCM fiber textile is made out of fibers disposed of in grids or yarns, which are very weak when solicited out of their axial direction [64]. The two mentioned FRCM drawbacks can be overcome by the adoption of a lime-based mortar [65–69], which allows for chemical affinity with the masonry substrate [19,20,70], and by using chopped short fibers randomly dispersed in the mortar matrix, which offers a multi-directional response to seismic actions. The traditional FRCM technology is characterized by another limitation that appears when the reinforcement is applied at a large scale on masonry structures. The application process is shown in Figure 1 and is composed of three phases, i.e., (i) the inorganic mortar matrix is applied to the historical masonry as a thin layer (see Figure 1b), (ii) the textile fabric is applied to the fresh mortar layer through light pressure (see Figure 1c), (iii) a second and last mortar layer is applied to the fiber grid, which at this stage is completely embedded (see Figure 1d). The mentioned process is totally hand-made and consists of a very time consuming activity.

This study proposes a new material suitable for strengthening existing masonry structures, that is made out of chopped basalt fibers dispersed in a lime-based mortar. The mortar is shown in Figure 1e, and it can be applied all at once on the existing masonry support. The proposed mortar is characterized by high versatility. In fact, it can be used as internal and/or external reinforcement of existing masonry walls, or as an alternative for existing and new masonry joints for irregular and regular masonries. The topic concerning the application of the new basalt mortar at a vast scale on various structural typologies is very interesting, but it is out of the scope of this study. In fact, the goal of this paper is to mechanically characterize the basalt reinforced mortar at the material scale, assessing the effect of both the length and content of basalt fibers on the mortar's mechanical properties, in perspective of its application to masonry heritage structures. Two are the main features of the newly proposed mortar, aiming to respect a sustainable strategy for the repair works: (i) 30% of the aggregates composing the mortar mix design are recycled, resulting from

the ruins of the 2009 L'Aquila earthquake, and (ii) chopped fibers are made out of basalt, a natural material of volcanic origin.

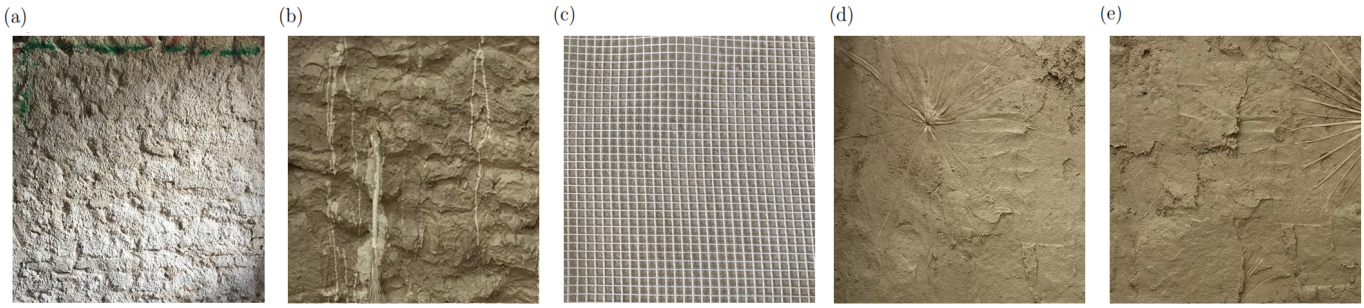

Figure 1. (**a**) Traditional unreinforced masonry panel. Ordinary FRCM strengthening system on masonry surface: (**b**) the first layer provides to apply a thin layer of plastering; (**c**) the second layer consists in applying the textile grid; (**d**) the third layer provides to apply a second and more massive layer of plastering. (**e**) Newly proposed FRCM retrofitting system on masonry wall: chopped basalt fibers are randomly placed within the mortar matrix: just one layer of mortar can be applied with a unique phase.

During recent decades, fibers made out of basalt have raised attention while being used in construction engineering [71,72] because of their low cost, non-toxicity, sustainability, and easiness of the production process (for a deeper comparison between basalt and other types of fibers, the reader is referred to [73,74]). Basalt fibers are produced from specific volcanic basalt rocks, namely acidic-type basalts, by means of a thermo-chemical process during which no additives are added. Continuous basalt fibers are then chopped into 12–20 μm diameters and into 3–240 mm lengths depending on the desired composite applications. Basalt fibers proved to be beneficial for enhancing the mechanical properties of several quasi-brittle materials [75–78]. In particular, several studies demonstrated a good improvement in the concrete mechanical properties when basalt fibers are used, both in cases where they are disposed of as rebars or grids on the external surface of concrete specimens or when the chopped basalt fibers are included within the concrete mix design [79–81]. In this latter case, Elshafie and Whittleston [82] showed that the concrete tensile strength significantly enhances by increasing the basalt fiber content or the basalt fiber length. Moreover, in the same study, it was shown that increasing the content or the length of basalt fibers in reinforced concrete improves its flexural strength, elastic modulus, and crack resistance. Other interesting studies pointed out the positive repercussions on the quasi-brittle behavior of cement-based mortar when basalt fibers are included [83–85]. Among other results, it was shown that mortar toughness augments when the fiber content grows, thus improving the resistance to deformation property and cracking.

The use of basalt fibers in concrete has already been widely addressed by several studies, but their incorporation within a restoration mortar for masonry architecture seldom appears in the literature. Mostly, a systematic assessment of both the length and content of basalt fibers on the mechanical behavior of restoration mortars remains unexplored, and it will be investigated in this study both experimentally and by means of regression analysis.

2. Materials and Methods

This section illustrates the materials, procedures, and test equipment adopted in the current experimental campaign for the definition of the mechanical properties of the proposed restoration mortar. Aiming to assess the influence of the length of fibers (FL) and content of fibers (FC) on the mechanical performance of the lime mortar strengthened with basalt fibers, two different FLs of 12 mm and 24 mm are used (both lengths are characterized by the same mechanical and geometrical properties), as shown in Figure 2. Nomenclature,

geometry (i.e., FL l_f, diameter of yarn d_f, and strand d_f^*) and mechanical properties (i.e., density ρ_f, Young's modulus E_f, tensile strength $f_{t,f}$, and ultimate strain $\varepsilon_{u,f}$) of both basalt FLs are reported in Table 1. The basic geometry of both basalt fibers consists of a single yarn, whose average diameter d_f is 0.014 mm. One of the last steps of the manufacturing process provided the application of a thick coating on basalt fibers, which is generally made out of zirconium dioxide (ZrO_2) and titanium dioxide (TiO_2) [83]. The coating process mainly aims to improve fiber durability when exposed to various chemicals, such as $Ca(OH)_2$ and NaOH. The value of the fiber diameter d_f^* after coating was not provided by manufacturers, and it was measured by means of an electronic micrometer. Thus, d_f^* represents an ideal fiber diameter, assuming the fiber cross-section to be perfectly circular.

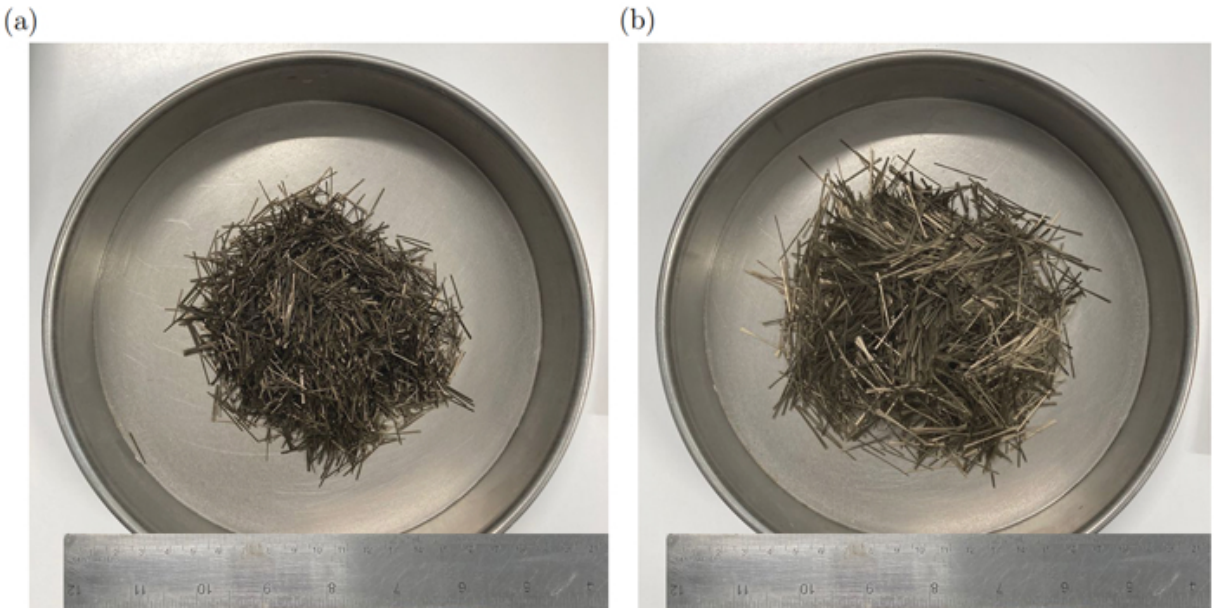

Figure 2. Chopped basalt plain fibers: (**a**) with short length equal to 12 mm and denoted by F12; (**b**) with long length equal to 24 mm and denoted by F24.

Table 1. Basalt fibers characterization: geometrical and mechanical properties.

Nomenclature	l_f [mm]	d_f [mm]	d_f^* [mm]	ρ_f [kg/m^3]	E_f [MPa]	$f_{t,f}$ [MPa]	$\varepsilon_{u,f}$ [%]
F12	12	0.014	0.030	2700	78,000	1800	4.2
F24	24	0.014	0.030	2700	78,000	1800	4.2

2.1. Mix Design

With the aim of evaluating the effect of the FL and FC on the mechanical properties of the lime-based mortar, both unreinforced and fiber-reinforced samples were prepared using the same mix design. Table 2 reports the components and the percentages by weight of the plain mortar conglomerate, consisting of a binder mixture, additives, aggregates, and water. For the mortar application to cultural heritage architectures, the percentage of lime must be a consistent part of the binder. In particular, the proposed mix shows a lime content equal to 70% of the binder weight, while the remaining 30% is Portland cement. The fraction of lime and Portland cement in the total weight of binders defines the mortar as "lime-based mortar", rather than "pure-lime mortar" [86]. The granular part consists of sand, with diameters ranging between 0.1 mm and 1.2 mm, while the content with respect to the whole weight of the product is equal to 65%. Finally, the water represents the 80% of the binder weight and the 20% of the whole product.

Table 2. Mix design composition: the first column indicates the categories, the second column the components, and the third column indicates the percentages in weight.

Category	Component	% [-]
Binders [1]	Lime	70
	Portland Cement	30
Aggregates [2]	Sand	65
Additives [2]	Fluidizer	0.2
	Resin	0.1
-	Water	80 [1], 20 [2]

[1] Compared to the binders weight. [2] Compared to the whole product weight.

2.2. Sample Preparation and Designation

Operationally, the two additives were first mixed, and then the binders and the sand-aggregate were incorporated into the dried mix, while water at room temperature was included as a last component during the mixing blending phase. After mixing all components in the mortar mixer for about 60 s, the mortar was poured into three molds of 160 × 40 × 40 mm in length, height, and depth, respectively, and then vibrated according to the standard code EN 1015-11 [87]. Each batch was first subjected to the slump test according to the detailed procedure described in the following section. Once the mortar was poured into molds, specimens were kept in the moist room for 48 h at a temperature of 20 °C (±2 °C) and a moisture content of 95% (±1%). At the end of the treatment in the moist room, samples were moved and kept for 26 days at 20° (room-temperature) and 60% of relative humidity. The testing procedure for the mechanical characterization of the samples took place after 28 days and is detailed in Section 2.4.

Fibers were added during the mixing phase as a second-to-last component, before the water. Since the aim of this study is to investigate the effect of the basalt content (FC) and length (FL) on the mechanical properties of the lime-based mortar, the experimental campaign involves six FC and two FL. In total, 36 strengthened samples are obtained, with a further three non-strengthened samples as a comparison group for a final test sample number equal to 39. For both short (12 mm) and long fibers (24 mm), the following FCs are analyzed: FC_{B1} = 0.50%, FC_{B2} = 0.75%, FC_{B3} = 1.00%, FC_{B4} = 1.50%, FC_{B5} = 2.00%, and FC_{B6} = 2.50%. Note that FC is the ratio of fiber weights to the whole product, so it is expressed as a percentage. Moreover, the highest percentage FC_{B6} = 2.50% is an upper bound for the mortar mixture corresponding to the maximum quantity embeddable in the conglomerate, since a greater percentage does not ensure the mixture's workability. For practical purposes, the ideal fiber content to be incorporated in mortar mixtures represents a fine balance between the maximization of fiber amount, to maximize the gain in terms of mechanical properties, and the containment of embedded fibers to avoid fiber segregation.

2.3. Workability

The workability is a fundamental characteristic of any cementitious mixtures, especially for industrialized materials to be produced on a large scale and put in place at worksites. Currently, the most common test able to evaluate the rheological properties of mortar and other cementitious materials in the fresh state is the slump test. The workability of the proposed mortar was characterized following the procedure described in EN 1015-3 [87] and ASTM C1437 [88]. In particular, the slump test consists of four phases: (i) casting the mortar in steel molds with a truncated cone shape, (ii) removing the cone in a vertical direction, avoiding rotational movement, straight up to clear the sample, (iii) tamping the

mortar with 20 strokes using Hagermann's table, (iv) using a ruler, measuring the mean diameter of the fresh mortar. Figure 3 shows the slump test procedure.

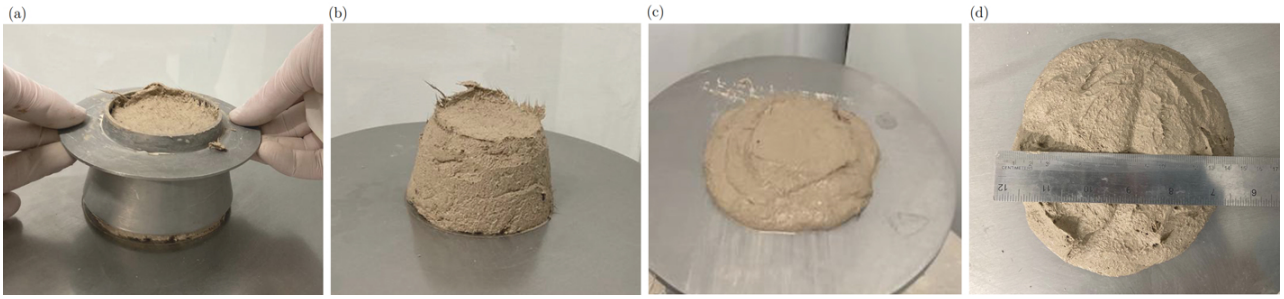

Figure 3. Four phases of the slump test: (**a**) casting the mortar in molds, (**b**) removing the cone along vertical direction, avoiding rotational movement, straight up to clear the sample, (**c**) tamping the mortar with 20 strokes using Hagermann's table, (**d**) using a ruler, measuring the diameter of fresh mortar as average of two orthogonal measurements.

2.4. Mechanical Characterization

All unreinforced and fiber-reinforced samples were tested after 28 days measured from the casting day [87]. The testing process aims to mechanically characterize the mortar samples in terms of flexural behavior and fracture energy, as well as in tension and in compression. The experimental campaign was carried out at the Laboratorio Prove Materiali e Strutture (LDPM) of the University of L'Aquila (Italy) by using the material testing machine "Zwick Roell".

2.4.1. Bending Behavior and Post-Peak Capacity

This section illustrates the three-point bending test (3PBT) carried out on the 39 samples, aiming to evaluate the mechanical performances in terms of flexural strength f_f and fracture energy G_f. Aiming to address the fracture in the middle of the specimen, before proceeding with the actual tests, a notch was fabricated using a manual precision saw on the entire set of specimens. Each notch has a 2 mm thickness and a 6 mm height, with a ratio between the notch and beam height a/d equal to 0.15 [63]. The testing setup of the notched samples tested in 3PBT is shown in Figure 4a,b. The two sample supports are placed at a distance L of 100 mm and provide constraints against vertical displacements, allowing instead horizontal ones. The test was conducted with a force P applied at the top middle length of the sample under displacement control conditions, with a constant velocity of 0.5 mm/min. The load P on the sample and the vertical displacement δ corresponding to the same mid-span point were measured and automatically recorded. Once stored, these data are used to compute the flexural stress σ_f using the following formula based on the theory of elasticity:

$$\sigma_f = \frac{3PL}{2b(d-a)^2} \tag{1}$$

where b and d are the width and the height of the specimen cross section, respectively. Once the load P reaches the maximum value ($P = P_{MAX}$), Equation (1) provides the bending resistance f_f supported by the mortar sample.

Aiming to evaluate the property of the tested material on energy dissipation, the fracture energy G_f was also computed. One of the most widely known methods is the 'work-of-

fracture' method, described in the RILEM recommendations [89–91]. The fracture energy G_f can be calculated by resorting to:

$$G_f = \frac{W_0 + mg\delta_0}{(d-a)b} \quad (2)$$

where W_0 is the area under the load–deflection curve, m is the weight of the specimen related to the volume included between the two vertical supports, g is the acceleration of gravity, and δ_0 is the deformation corresponding to the specimen failure conditions.

After performing the bending test, each of the 39 specimens was bisected and used for the subsequent tests, i.e., for the splitting test and the compression test. Thus, 39 specimens were again tested in tension and compression.

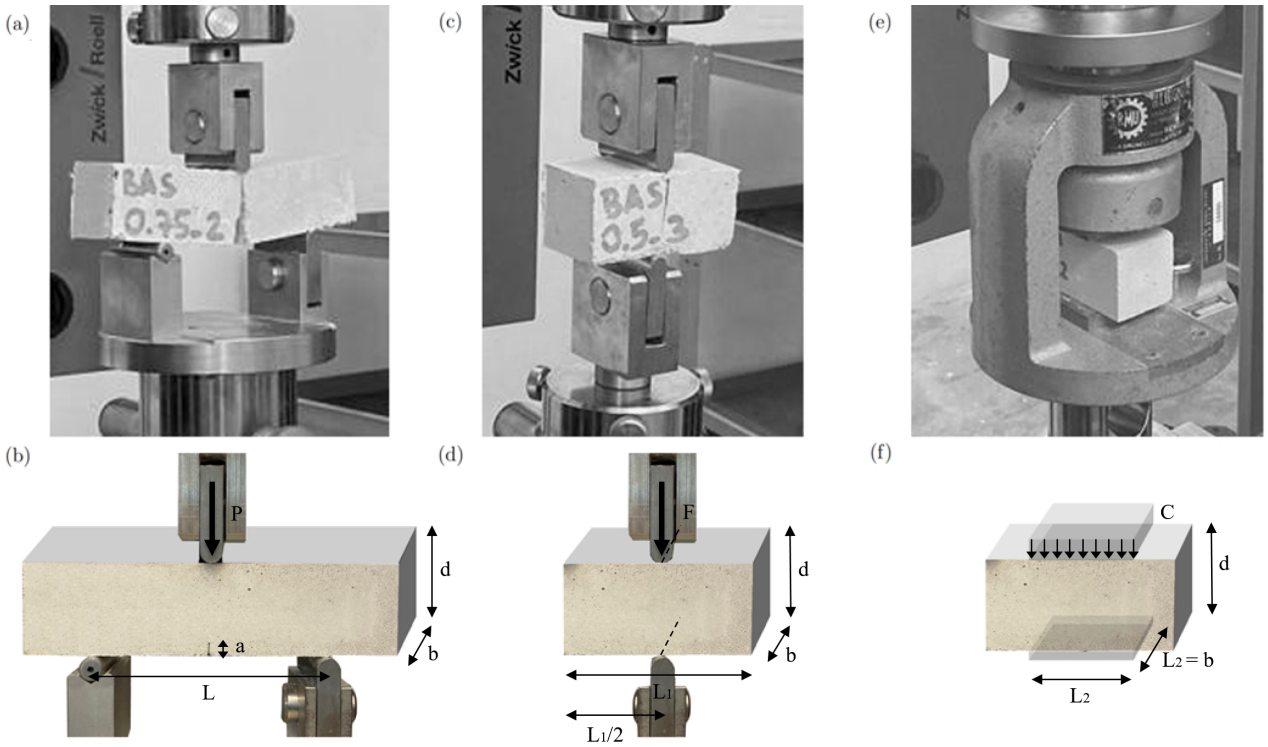

Figure 4. Testing equipment and structural configurations for: three-point bending test in (**a**,**b**), splitting (or Brazilian) test in (**c**,**d**), compressive test in (**e**,**f**).

2.4.2. Tensile Behavior

In this section, the splitting tests (ST) are presented. This destructive test (indifferently called the Brazilian test) implies an indirect method of measuring the tensile properties of materials. In comparison with other tensile test procedures, ST is easier to perform, and the data scattering is statistically lower. Moreover, ST does not require the samples to have a unique shape, as most of the testing protocols allow the use of specimens characterized by diversified shapes.

Aiming to measure and compare the tensile resistance in strengthened and non-strengthened configurations, the ST was performed on 40 mm × 40 mm × 80 mm prismatic specimens obtained from the two half specimens representing the broken pieces of the 3PBT, as shown in Figure 4c. ST provides the sample to be subjected to two opposite compressive loads, as depicted in Figure 4d. The application of the two antipodal compressive loads, vertically oriented, generates a tensile force (and thus stresses) in a perpendicular direction, hence horizontally oriented. When the internal tensile stresses exceed the tensile strength of the material, a crack triggers at the geometrical center of the sample, in accordance with

Griffith criterion [92]. It should be noticed that when the fracture does not occur in the specimen's geometrical center, the ST is not valid, and the corresponding results cannot be considered representative of the sample's tensile resistance. As already performed in 3PBT, the ST was conducted with a force P applied at the top middle length of the sample, imposed with a constant velocity equal to 0.5 mm/min. In the same application point of P, the vertical force F and the vertical displacement δ are measured and automatically recorded at each iteration time. Therefore, the following equation was used to calculate the tensile stress: σ_t:

$$\sigma_t = \frac{2F}{\pi bd} \tag{3}$$

It is worth observing that when $F = F_{MAX}$, the value of the vertical force F reaches its maximum; therefore, Equation (3) allows us to compute the tensile resistance f_t supported by the prismatic mortar sample.

2.4.3. Compressive Behavior

For the definition of the compressive resistance of the mortar samples, the compressive tests (CT) in unconfined conditions were carried out for both non-strengthened and fiber-strengthened configurations. Each sample measuring 40 mm × 40 mm × 80 mm was obtained from the two broken pieces resulting from the 3PBT (see Figure 4e). The CT were carried out on a total number of 39 specimens, arranged and loaded as shown in Figure 4f. Each specimen was placed with the bottom face on a squared area of 40 mm × 40 mm, while on the top squared area (measuring 40 mm × 40 mm) of the specimen, the distributed load C was applied. As already done for the two previous tests, the CT were carried out in displacement control with a displacement rate equal to 1 mm/min. Finally, the parameters C and δ, i.e., the applied load and the corresponding vertical displacement, were recorded in real time by the dedicated software. After the CT performance, the compressive stress σ_c was computed based on:

$$\sigma_c = \frac{C}{bL_2} \tag{4}$$

When $C = C_{MAX}$, the value of the vertical load C reaches its maximum. Equation (4) allows us to calculate the compressive resistance f_c supported by the prismatic mortar sample. In addition, knowing the vertical displacement at the mid-span point δ, the vertical strain ε_v can be computed using the following equation:

$$\varepsilon_v = \frac{\delta}{d} \tag{5}$$

3. Experimental Results

The experimental results on both mortars, i.e., non-reinforced and basalt fiber-reinforced, are examined in this section. In particular, the first three sections (namely Section 3.1, Section 3.2, and Section 3.3) report the results for the 3PBT, ST, and CT, respectively. Section 3.4 reports a synthesis of the results and a discussion. Finally, the slump test results are shown in Section 3.5, and the cruciality deriving from the workability of the conglomerate is discussed.

3.1. Flexural Strength and Post-Peak Capacity

The behavior in bending for different contents and lengths of basalt fibers is illustrated in Figure 5, which depicts all the curves on the flexural stress versus displacement plot. From this figure ahead, short and long FRCM samples (named F12 and F24) are marked with red and orange curves, respectively. The unreinforced cases' results are reported in Figure 5f with gray lines. The analyzed cases characterized by a different fiber con-

tent, i.e., FC_{B1} = 0.50%, FC_{B2} = 0.75%, FC_{B3} = 1.00%, FC_{B4} = 1.50%, FC_{B5} = 2.00%, and FC_{B6} = 2.50%, are progressively shown starting from the upper left side of Figure 5.

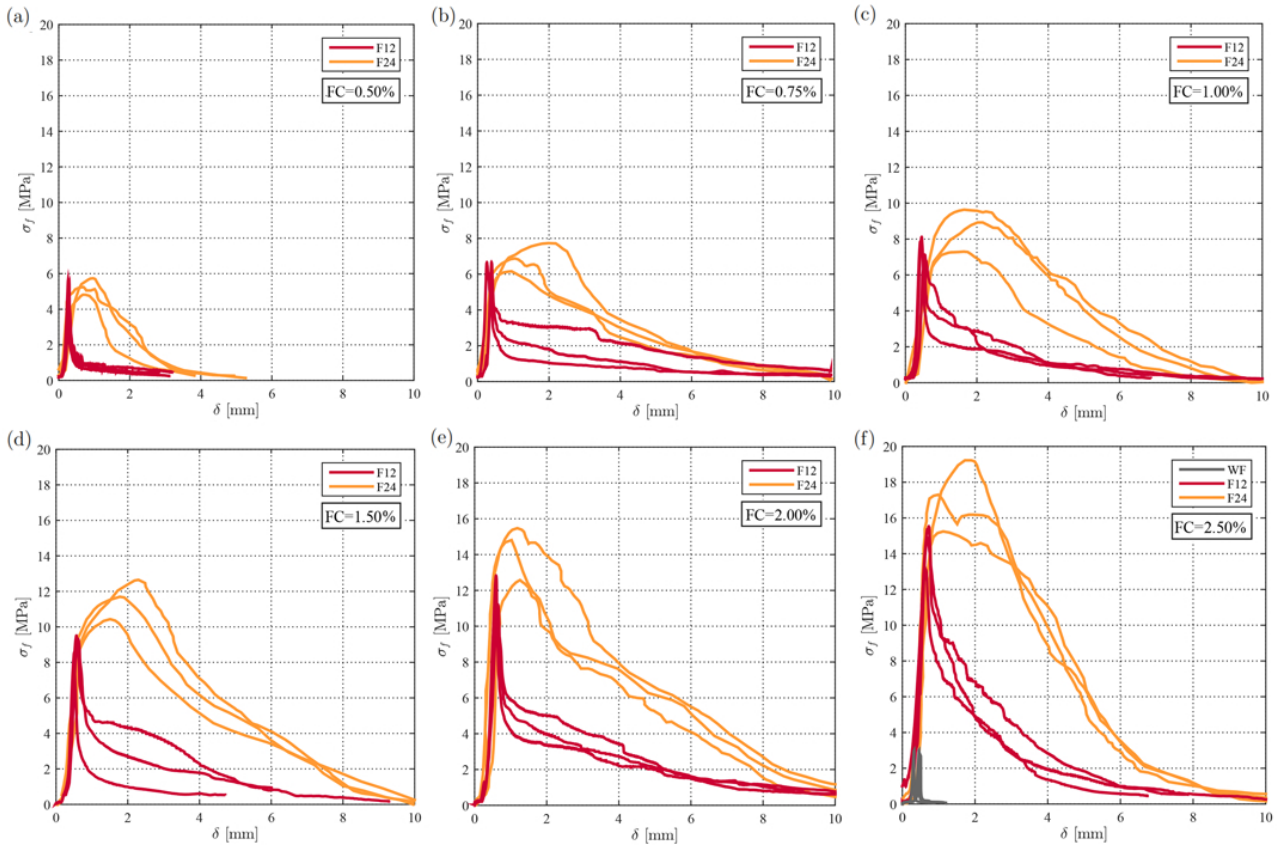

Figure 5. Flexural behavior for short fibers in red and long fibers in orange and for the following fiber contents: (**a**) FC = 0.50%, (**b**) FC = 0.75%, (**c**) FC = 1.00%, (**d**) FC = 1.50%, (**e**) FC = 2.00%, and (**f**) FC = 2.50%. The flexural capacity increases with fiber content FC and fiber length FL.

A general trend can be observed in terms of flexural behavior: The flexural strength f_f rises as the content of fibers is augmented. Figure 5f points out that unreinforced specimens have a flexural strength f_f equal to about 3 MPa, which is much lower than the cases characterized by fibers of long and short lengths at the maximum content, namely F24-FC_{B6} and F12-FC_{B6}, for which f_f turns out to be about 19 MPa and 15 MPa, correspondingly. For fiber contents ranging from FC_{B1} to FC_{B5}, the peaks f_f increase monotonically with the FC, and they are bounded between the smaller and the higher values corresponding to the without the fiber case and the FC_{B6} case, respectively. This result is due to the positive correlation between the fiber number encountered during the rupturing process along the fracturing path and the fiber content FC: the higher the fiber number, the higher the sample's flexural capacity. Also, the fiber length proved to enhance the sample's bending capacity. In fact, the flexural strength is higher for the long FRCM samples (F24 cases) than for the short ones (F12 cases). This occurs for all the FCs with the exception of the FC_{B1} case. A plausible explanation of this latter exception is that, for a low fiber content, the number of fibers encountered in the fracturing path is very limited and, as a result, the fiber length contributes to the overall flexural capacity in a negligible manner.

Most importantly, the long FRCM samples (F24 cases) exhibit a more pronounced ductility with respect to the F12 cases (the reader can qualitatively compare the areas subtended by the red and orange load-deflection curves in Figure 5a–f). A deeper quantitative discussion is performed in Section 3.4, which physically explains the correlation between the fracture energy G_f and the FL. Unreinforced WF samples are characterized by a purely brittle behavior, as all sample failures occur all at once and very suddenly, generating almost vertical post-peak curves.

3.2. Behavior in Tension

Figure 6 shows the ST results for both the non-reinforced and basalt FRCM cubes. In particular, it illustrates the mortar tensile behavior in terms of tensile stress σ_t versus displacement δ curves. The tensile behavior is depicted for all the FC and both the investigated lengths of fibers, marked by red and orange solid lines. Figure 6f also shows the results related to the unreinforced case (WF case), denoted by gray curves in the plot. The WF tensile behavior is very brittle, as samples reach the tensile peak and instantaneously fail with no softening capacity. All six analyzed cases, characterized by a specific content of fibers, i.e., FC_{B1} = 0.50%, FC_{B2} = 0.75%, FC_{B3} = 1.00%, FC_{B4} = 1.50%, FC_{B5} = 2.00%, and FC_{B6} = 2.50%, are shown progressively from the top left corner in Figure 6.

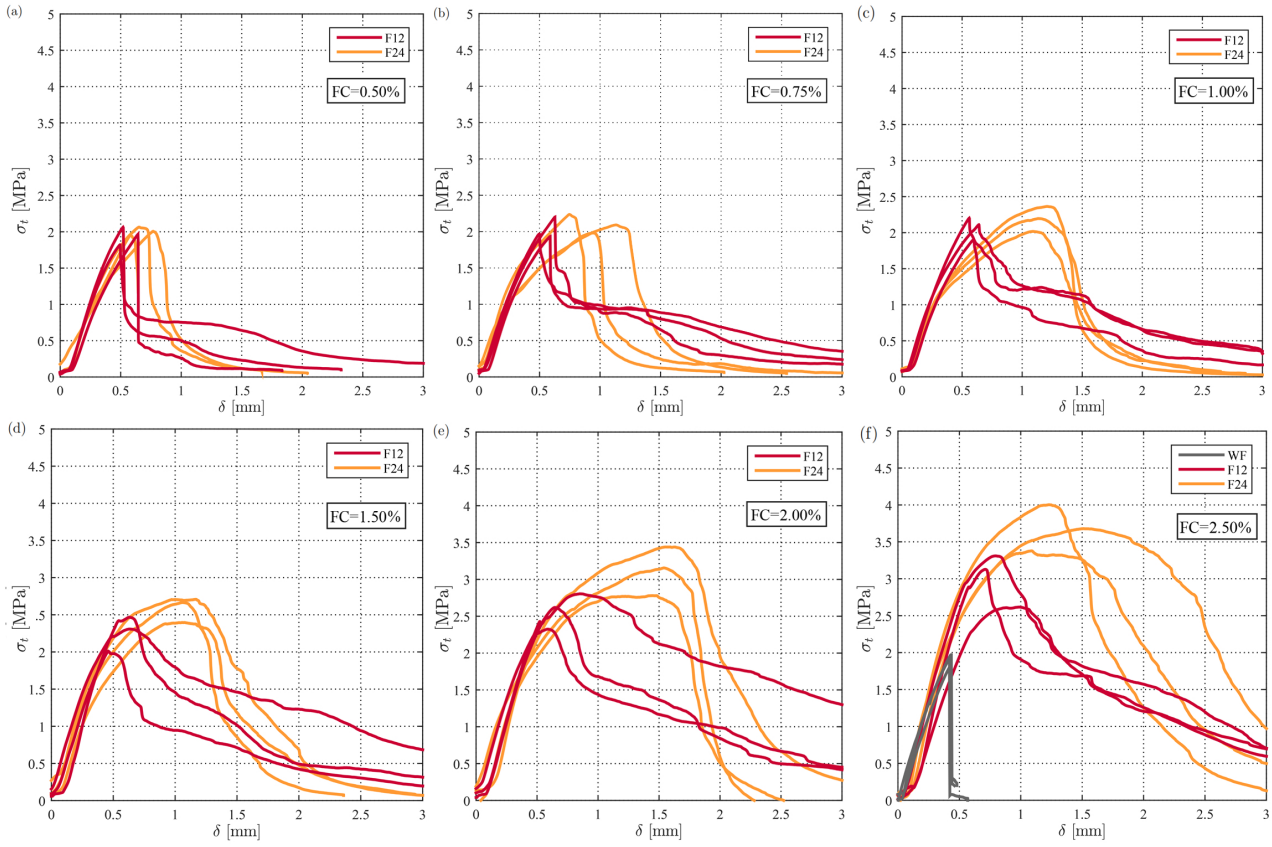

Figure 6. Tensile behavior for short fibers in red and long fibers in orange and for the following fiber contents: (**a**) FC = 0.50%, (**b**) FC = 0.75%, (**c**) FC = 1.00%, (**d**) FC = 1.50%, (**e**) FC = 2.00%, and (**f**) FC = 2.50%. The tensile capacity increases with FC and FL.

Analogously to 3PBT results, the results related to the ST show that the tensile strength f_t increases when the FC is augmented. In fact, the tensile strength f_t related to the WF sample is equal to about 2 MPa (the reader is referred to Figure 6f), whereas f_t related to the cases reinforced with the maximum fiber content and short fibers is equal to 3.25 MPa (F12-FC$_{B6}$ cases), and f_t related to the cases reinforced with the maximum fiber content and long fibers is equal to 4 MPa (F24-FC$_{B6}$ cases).

Additionally, the in-between fiber contents (FC$_{B1}$ to FC$_{B5}$) are characterized by f_t, which progressively increases with the FC. Moreover, the tensile strength f_t increases while augmenting the FL. This result applies to all the FC, except for the FC$_{B1}$ and FC$_{B2}$ cases, with the tensile strength being higher for the long fiber reinforced cases (F24 cases) than for the short fiber reinforced ones (F12 cases).

Plausible reasons for this observation are similar to those drawn in 3PBT: for a low fiber content, the number of fibers involved in the fracture along the ligament is also very low and, thus, the contribution of the fiber length to the overall tensile capacity is not appreciable. Also, in tension and for all the FC, the long FRCM samples (F24 cases) show a greater post-peak capacity when compared with the F12 cases, as shown in Figure 6. Aiming to provide a physical explanation for the increase in post-peak capacity with the FL, one should resort to the fiber-mortar adhesion surface that resists the fracturing process. The adhesion surface is higher for long fiber samples than for small fiber ones, and therefore they better resist the cracking propagation phenomenon, increasing the overall post-peak capacity at all the FC.

3.3. Behavior in Compression

The results related to the mechanical behavior in compression are depicted in Figure 7. The curves are related to different conditions for FC and FL, and they are shown in terms of compressive stress σ_c versus vertical strain ε_v in the various plots. In all figures, the red and orange lines denote the experimental data for small-length and big-length FRCM samples. The bottom right figure, i.e., Figure 7f, additionally shows the experimental data for the non-reinforced cases (WF cases). Once again, the compressive behavior is very brittle, and one assists with a sudden collapse of all the samples once the compressive strength is reached. Also, a positive correlation between compressive strength and fiber content can be pointed out: f_c enhances as the FC augments. This result is very clear if one compares the F24-FC$_{B6}$ and F12-FC$_{B6}$ cases (enriched by big and small fibers at the highest content) with the plain mortar case (WF case): for the latter cases the average f_c is about 17.5 MPa, whereas for the former ones, it is 30 MPa and 28 MPa, respectively. For median FC, the compressive capacity progressively increases with the FC, going from the WF case up to the FC$_{B6}$ case. The compressive behavior depends on the fiber length in an analogous way to both the flexural and tensile behaviors: the compressive strength f_c rises as the FL is augmented. However, it is worth underlining that the f_c correlates with FL in a milder way when compared to both the tensile and flexural properties. This appears clear if one observes the f_c related to FC$_{B1}$, FC$_{B2}$, and FC$_{B3}$ cases, for which the mean f_c are quite similar, as opposed to the FC$_{B4}$ case and above, for which the dependence of f_c on the FL appears progressively more pronounced. Therefore, the fiber length FL plays a milder role in compression than the fiber content FC; in compression, the fiber number is more important than the fiber length.

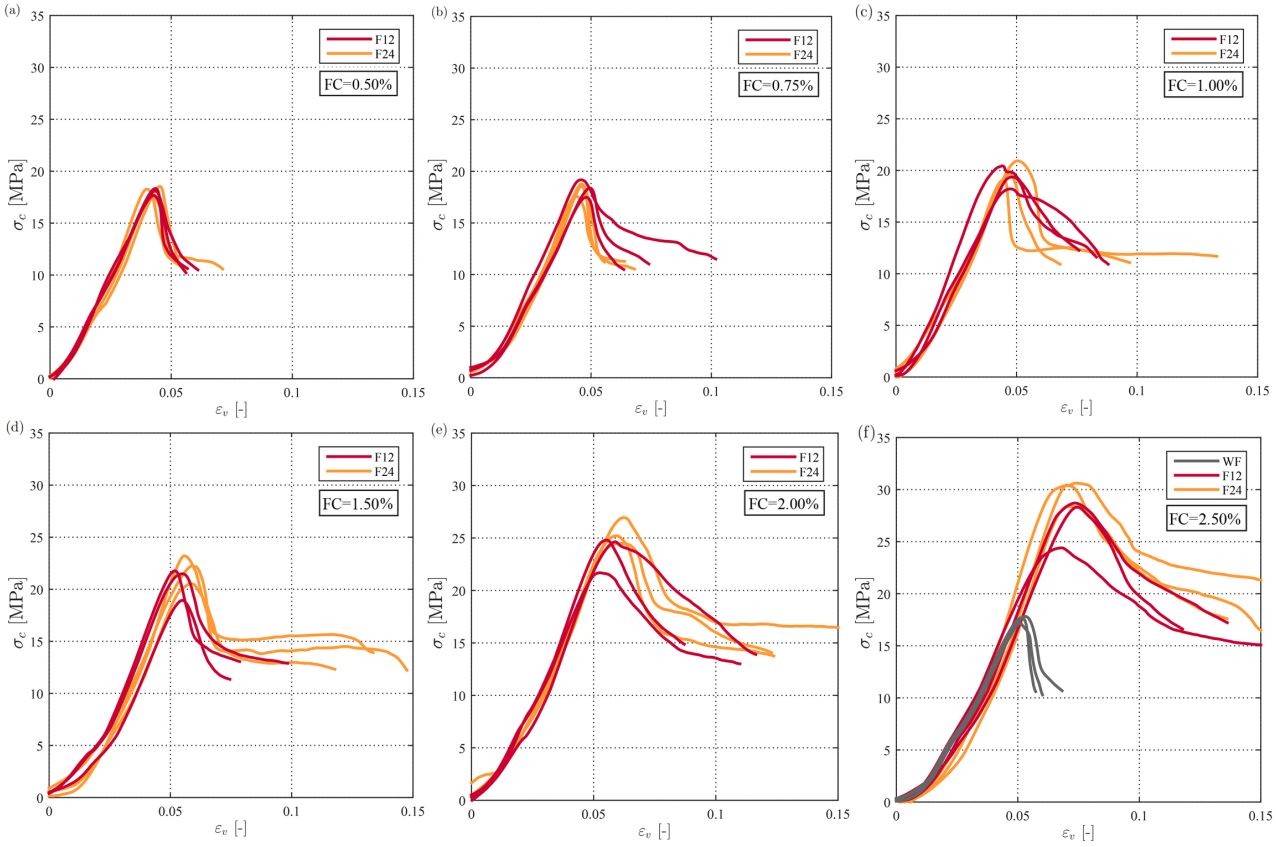

Figure 7. Compressive behavior for short fibers in red and long fibers in orange and for the following fiber contents: (**a**) FC = 0.50%, (**b**) FC = 0.75%, (**c**) FC = 1.00%, (**d**) FC = 1.50%, (**e**) FC = 2.00%, and (**f**) FC = 2.50%. The compressive capacity increases with FC, but it does not change appreciably with the fiber length.

3.4. Discussion

The aim of this paper is to understand the effect of basalt fiber content FC and fiber length FL on the mortar's mechanical properties. Figures 8 and 9 are elaborate to guide the reader in this direction and to summarize the obtained results. In particular, Figure 8 reports four synthetic histograms that clarify how all the mortar's mechanical properties are enhanced by basalt FC and FL. From top left, Figure 8 shows the trends of the flexural strength, the fracture energy, the tensile strength, and the compressive strength versus the fiber content for different fiber lengths (the reader is referred to Figure 8a, Figure 8b, Figure 8c, and Figure 8d, respectively). It is important to recall that, in order to compute f_f, G_f, f_t, and f_c, Equation (1), Equation (2), Equation (3), and Equation (4) are respectively used.

Generally, it is worth underlining that the main basalt fiber effect is to enhance all the analyzed mechanical properties; this occurs for all the contents and lengths of fiber. Analyzing the tensile strength related to the sample reinforced with long fibers and maximum FC (F24-FC$_{B6}$ case), one can notice an increase of more than 90% compared with the unreinforced mortar (WF case). In this same case, the flexural strength shows a great enhancement, increasing by more than 690% with respect to the WF case. The enhancement of the mortar's mechanical properties is very relevant in the perspective of its application at the structural scale. In particular, the enhancement of the tensile strength is important for the seismic retrofitting of heritage buildings, which are prone to show diffuse damage and collapse when subjected to seismic loads [93]. Authors have recently shown the effectiveness of the basalt-enriched mortar applied to one-head and two-head masonry structures [94,95]. One of the mechanical properties that is mostly augmented because

of the fiber's beneficial effects is the fracture energy G_f, which exceeds an increment of 2230% for the same mentioned case (F24-FC$_{B6}$ case compared with the WF case). The increase in fracture energy is of paramount importance when aiming to reinforce structures located in seismic areas because it increases the structural capacity of dissipating energy in a non-linear regime through extensive fracturing patterns before the partial or overall collapse [96–98]. On the contrary, the mechanical parameter less sensitive to fibers, and above all their length, is the compressive strength, which shows a magnification of just about 72% (comparison between the F24-FC$_{B6}$ case and WF the case).

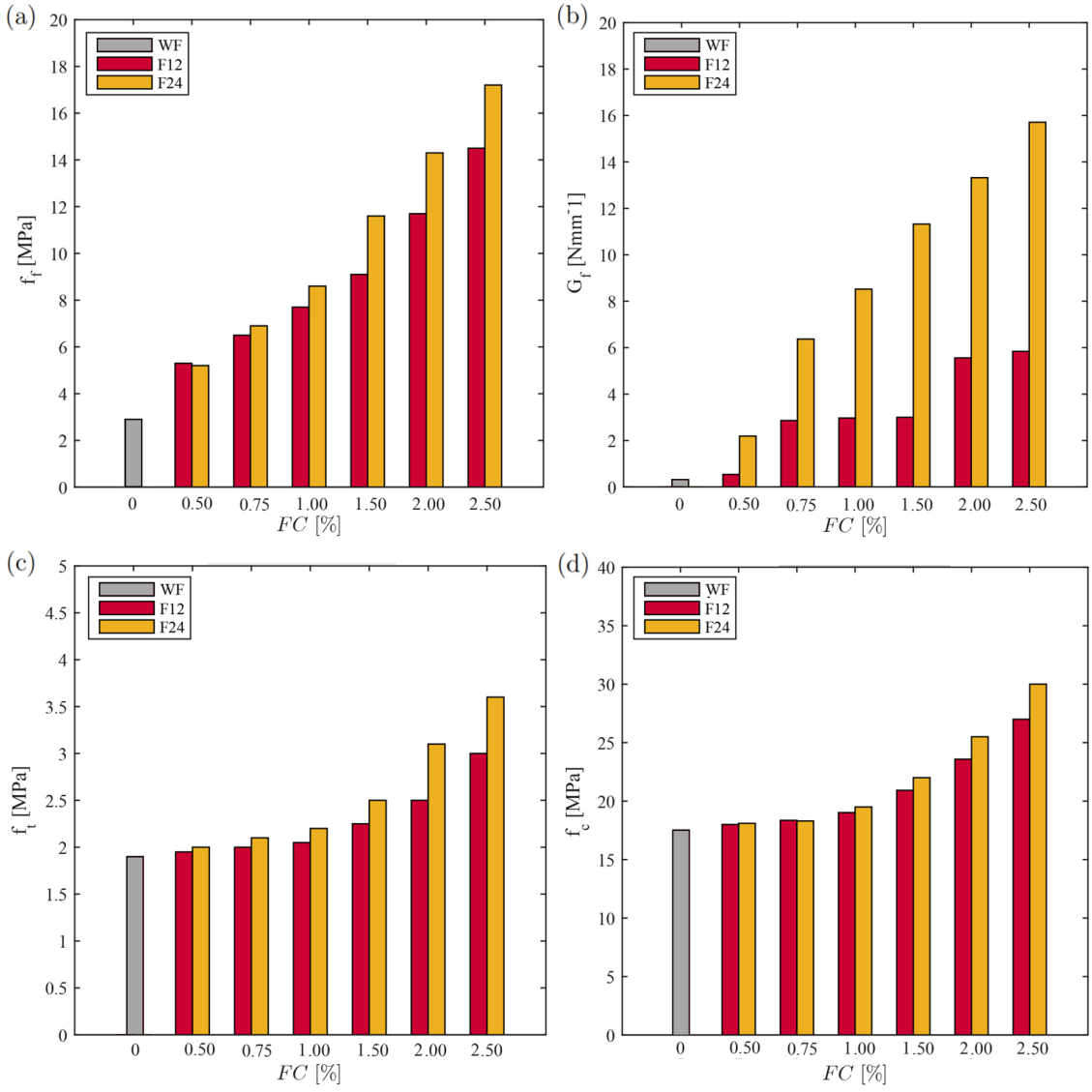

Figure 8. Synthetic figure showing the trend of all the analyzed mechanical properties versus the content of basalt fibers for the three different situations of no fibers, low length fibers, and high length fibers: (**a**) flexural strength versus content of basalt fibers, (**b**) fracture energy versus content of basalt fibers, (**c**) tensile strength versus content of basalt fibers, and (**d**) compressive strength versus content of basalt fibers. Basalt fibers increase all the mortar mechanical properties, above all the fracture energy.

Figure 9 shows the role played by the length and the content of basalt fibers on the scattering of experimental results. As a general trend, it can be noticed that the scattering increases as the FC increases. More specifically, the dispersion of flexural strength s_{f_f} increases by increasing both the FC and FL, as shown in Figure 9a. For the tensile behavior,

the fact that the FC is responsible for increasing the dispersion of experimental data s_{f_t} can be observed in Figure 9c. In the same plot, one can see that s_{f_t} is higher when mortar samples are enriched by long fibers rather than short ones, and this occurs for all cases except for FC_{B5} = 2.00%. Also in compression, the experimental data scattering s_{f_c} increases with the increment of FC, as shown in Figure 9d. For the compressive behavior, the s_{f_c} is higher for long fiber samples F24 up to FC_{B2} = 0.75%. From FC_{B3} = 1.00% and above, s_{f_c} is greater for mortar test pieces strengthened by small fibers. Finally, Figure 9b shows that there is no dependence of the fracture energy scattering s_{G_f} on both the fiber content and fiber length.

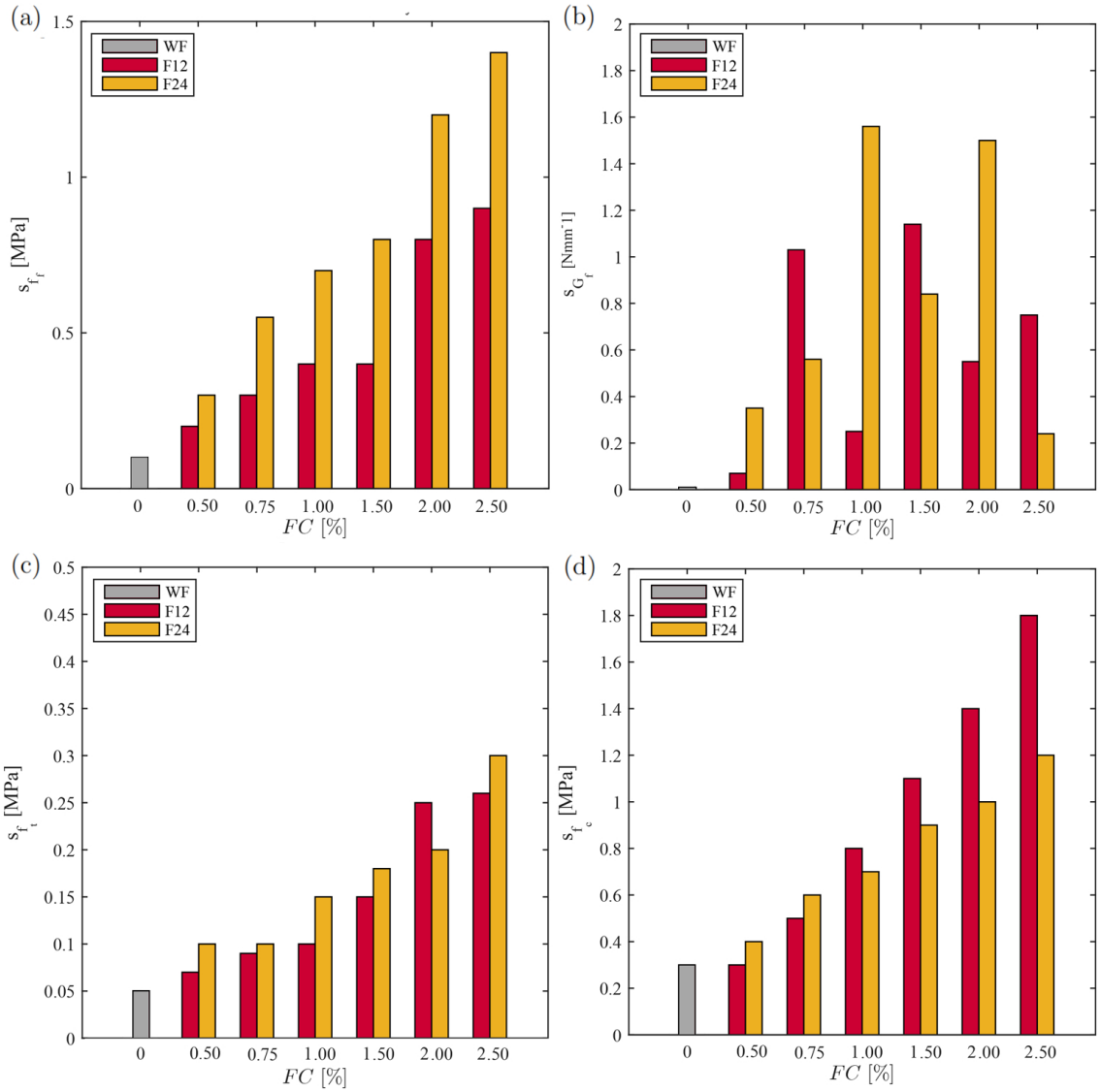

Figure 9. Synthetic figure showing the trend of the scattering related to all the analyzed mechanical properties with the fiber content and the fiber length: (**a**) scatter of flexural strength, (**b**) scatter of the fracture energy, (**c**) scatter of the tensile strength, and (**d**) scatter of compressive strength.

Generally, the presence of basalt fibers increases the overall randomness in the distribution of the mechanical properties of the reinforced mortar compared with the ones related to the non-reinforced case. This is demonstrated by the higher values of data scattering for all the reinforced specimens with respect to the non-fiber ones. This observation applies to all the analyzed fiber contents and fiber lengths and for all the considered behaviors, i.e., flexural, tensile, and compressive behaviors.

3.5. Optimization of the Basalt Reinforced Mortar Based on Its Fresh State Properties

The slump test procedure was described in Sections 2.2 and 2.3. The results of the slump test performed on all mortar batches are illustrated in Figure 10, which reports the slump versus the fiber content in cases of short and long basalt fiber reinforcement. A univocal trend can be traced: the increase in fiber content generates an almost linear decrease in the slump value. This implies that in both long and short fiber mortars, the fiber's incorporation within the mortar mixture reduces its workability and therefore negatively affects the conglomerate properties in the fresh state. Also, the slump value is lower for mortar reinforced with long fibers as opposed to short fibers. This demonstrates that mixtures enriched with short fibers are more workable than long fiber mixtures, and therefore the first ones are preferable for practical purposes.

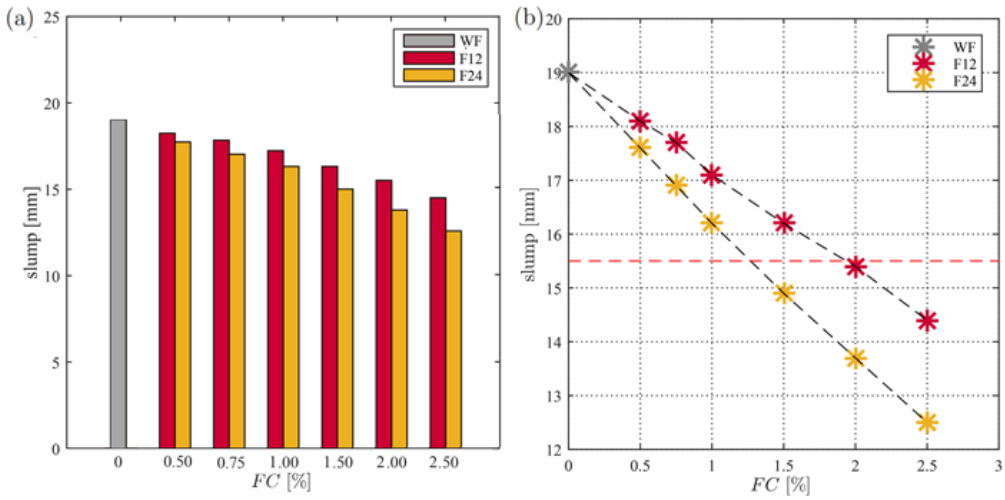

Figure 10. (**a**) Values related to the slump test for no fiber batches, short basalt fiber batches in red, and long basalt fiber batches in orange. (**b**) slump value as a function of the fiber content for both short and long fiber mortars: slump decreases almost linearly with the fiber content for both the fiber lengths. The red dashed line individuates the minimum slump value of 15.5 mm for practical purposes.

The results obtained in the previous sections are related to mortar specimens in the hardened state. We showed that the main fiber effect is to enhance all the mortar's mechanical properties. This result wrongly suggests that the best retrofitting mortar is characterized by the highest fiber content and the highest fiber length. In fact, the best engineering solution must satisfy the essential requirement of workability. In this way, the restoration mortar can actually be applied to the existing surfaces on a large scale. In this perspective, it is important to point out several practical considerations that the mortar must satisfy when applied to extensive surfaces: the conglomerate at the fresh state cannot slide when subjected to its own load; the workmanship must have the possibility of applying the mortar mixture not instantaneously but in successive layers; the mortar consistency should allow the mix to be sprayed (and not hand-applied) on the existing surfaces, aiming to reduce the workmanship costs and speed up the construction times. How do we ensure the satisfaction of the workability requirement and, implicitly, of mentioned considerations? The slump value should not be less than about 15.5 mm. Figure 10b shows the two cases for which the aforementioned condition is met: the F24-FC_B = 1.2% case, for which the basalt long fibers are at a fiber content equal to 1.2%, and F12-FC_B = 1.9% case, which implies the inclusion of basalt short fibers at a fiber content of 1.9%.

4. Regression Analysis

The aim of this section is to derive regression expressions for the four mechanical parameters f_f, G_f, f_t, and f_c calculated by means of the previous tests, for both cases of short and long fibers. This allows us to individuate an average trend for each mechanical property within its observation domain. For all cases, the matching accuracy between experimental data and regression curves is calculated by means of the coefficient of determination r^2 [99,100]:

$$r^2 = \frac{[\sum_{i=1}^{n}(y_i - \bar{y})(\hat{y}_i - \bar{\hat{y}})]^2}{\sum_{i=1}^{n}(y_i - \bar{y})^2 \sum_{i=1}^{n}(\hat{y}_i - \bar{\hat{y}})^2} \quad (6)$$

In this last equation, n is the specimen number, y_i is the i-th specimen's experimental parameter, $\hat{y}$ is the mean value of the experimental parameter, while $\hat{y}_i$ and $\bar{\hat{y}}$ are the i-th specimen's calculated parameter and the mean value of the calculated parameter, respectively. The coefficient r^2 provides an estimate of the fitting accuracy, and it ranges between 0 and 1. In this study, we consider one linear and two non-linear regression models for the regression analysis of the experimental data. In particular, we use the function $Y(X) = AX + B$ for the linear regression (LRL), the exponential function $Y(X) = Ce^{DX}$ for the exponential regression (ERL), and the quadratic function $Y(X) = MX^2 + N$ for the parabolic regression (PRL). It is worth underlining that regression functions are applicable within the variation domain of experimental data.

4.1. Bending and Post-Peak Behaviors

Two parameters of interest characterizing the mortar bending capacity are considered for the flexural regression analysis, i.e., the flexural strength f_f and fracture energy G_f. For both fiber lengths, we first compute the coefficients of determination for the three regression models, i.e., r^2_{LRL}, r^2_{PRL}, and r^2_{ERL}. Therefore, the highest r^2 is determined, and the best regression model for each parameter is identified. Figure 11a illustrates the r^2 related to the flexural strength f_f for the three different regression models and for short and long fiber mortars (in red and orange colors, respectively). As r^2_{LRL} is the highest for both short and long fibers (equal to 0.993 and 0.997, respectively), the linear regression model provides the best fitting for the parameter f_f. A linear regression function $f_f(FC) = A_{FL}FC + H_{FL}$ is therefore associated with both fiber lengths, where A_{FL} and H_{FL} are the pair of regression constants for each fiber length. Figure 11b shows these equations for the F12 case (red dotted line) and the F24 case (orange dotted line). For the F12 case, the regression constants A_{12} and H_{12} are equal to 4.6 and 2.9 MPa, and for the F24 case A_{24}, H_{24} are equal to 5.7 and 2.9 MPa. Therefore, replacing appropriately, for short fibers mortar $f_{f,F12} = 4.6FC + 2.9$ and for long fibers mortar $f_{f,F24} = 5.7FC + 2.9$. It is interesting to note that the pair of values H_{12} and H_{24} not only coincide but are also very similar to the value of the average flexural strength of the unreinforced mortar $f_{f,0}$ (see Figure 8a). Moreover, comparing the two angular coefficients A_{12} and A_{24}, depicted with red and orange dotted lines in Figure 11b and respectively equal to 4.6 and 5.7, one can notice an additional dependency on the FL. In fact, A_{FL} for long fibers is greater than for short fibers ($A_{24} > A_{12}$), implying a greater flexural strength f_f of the long fiber samples for the entire range of variation of the FC.

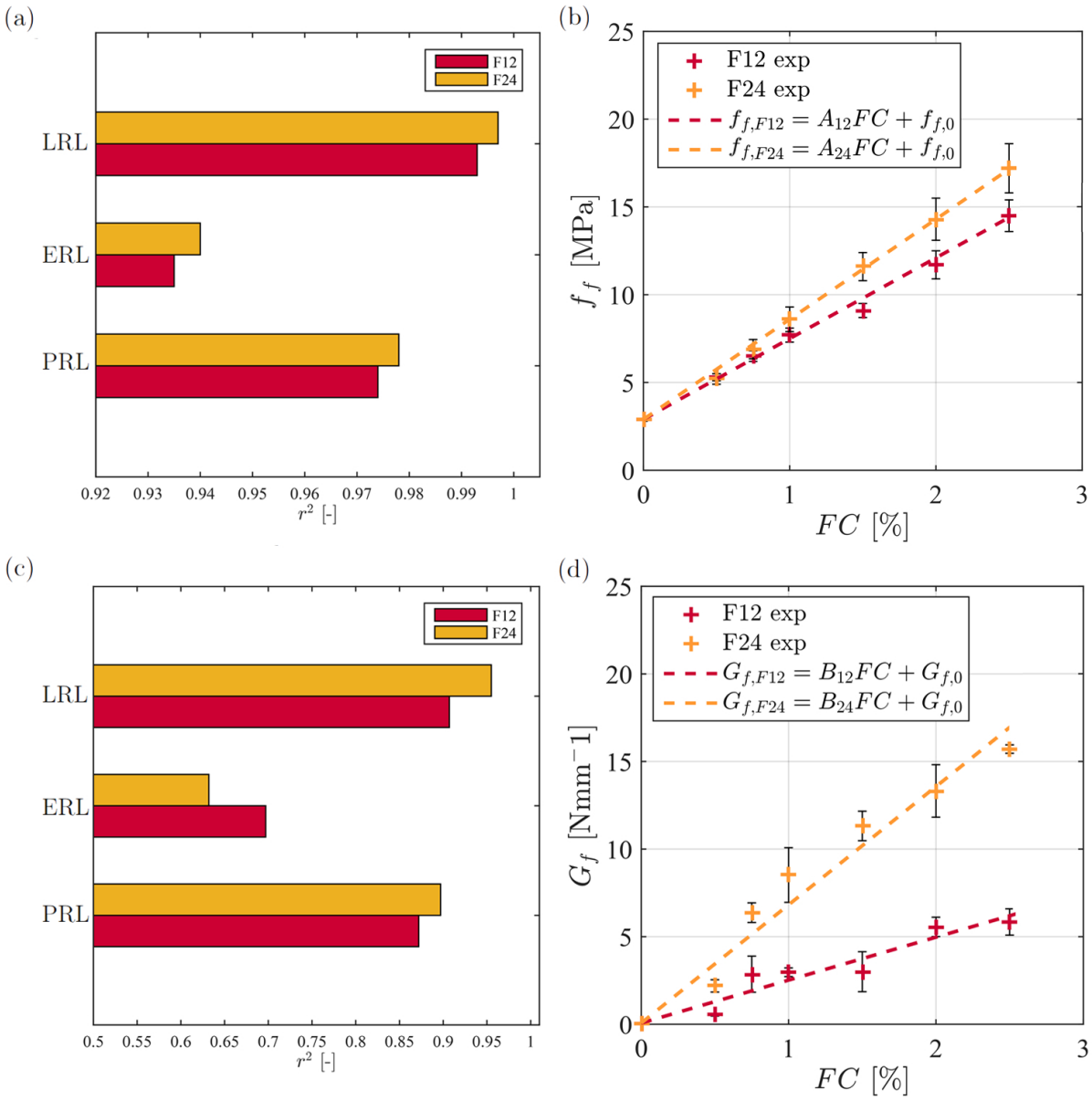

Figure 11. (**a**) coefficients of determination r^2 for the flexural strength calculated for the LRL, ERL, and PRL, for both short and long basalt fibers; (**b**) flexural behavior regression lines as a function of the fiber content; (**c**) coefficients of determination r^2 for the fracture energy calculated with the three mentioned regression models, i.e., with LRL, ERL, and PRL; (**d**) fracture energy regression lines as a function of the fiber content.

The regression analysis for the fracture energy G_f is similar to that performed for the flexural strength. Figure 11c shows the regression coefficients r^2_{LRL}, r^2_{ERL}, and r^2_{PRL} for the two mortar fiber lengths. With r^2_{LRL} equal to 0.907 and 0.955 for short and long fiber mortars, the linear regression model best describes the mortar behavior, and the function $G_f(FC) = B_{FL}FC + L_{FL}$ is the fitting function for both lengths. In this equation, B_{FL} and L_{FL} are regression constants for a given FL. Figure 11d shows the linear equations related to F12 (red dotted line) and F24 (orange dotted line) mortar samples. In the first case, the coefficients of regression B_{12} and L_{12} are equal to 2.45 and 0.07 Nmm^{-1}, respectively. For the second case B_{24}, L_{24} are equal to 6.75 and 0.07 Nmm^{-1}, respectively. Therefore, replacing appropriately, for the short fibers, the function is $G_{f,F12} = 2.45FC + 0.07$, while for the long fibers it is $G_{f,F24} = 6.75FC + 0.07$. It is interesting to point out that the pair of values H_{12} and H_{24} not only coincide but are also very similar to the value of the

average flexural strength of the unreinforced mortar $f_{f,0}$ (see Figure 8a). Comparing the two angular coefficients L_{12} and L_{24}, they both are small and very close to the fracture energy computed for the case of the plain mortar $G_{f,0}$ (see Figure 8b). From this numerical evidence, the regression coefficient L_{FL} does not depend on FL, and it can be set as null. The latter assumption provides, on one hand, analytical evidence regarding what was already experimentally observed in Section 3.1 about the brittle behavior of the mortar specimen for the not-strengthened configuration; on the other hand, it explains why the fracture energy is often neglected by manufacturers and practitioners engineers. Unlike the case of unreinforced mortar, the fracture energy is one of the main parameters to be considered for fiber-reinforced mortars, as it estimates the mortar capacity of dissipating energy in the post-elastic regime, especially if long fibers are used. In fact, by comparing the two angular coefficients B_{12} and B_{24}, depicted with red and orange dotted lines in Figure 11d and respectively equal to 2.45 and 6.75, one can notice a greater value of B_{FL} for long fibers ($B_{24} > B_{12}$), implying a greater fracture energy G_f of the long fibers specimens for the entire range of variation of the FC.

4.2. Tensile Behavior

The regression analysis related to the tensile behavior is performed on the tensile strength f_t. Figure 12a shows the three regression coefficients r^2_{LRL}, r^2_{ERL}, and r^2_{PRL} for F12 and F24 cases. r^2_{PRL} is equal to 0.996 for the short fibers mortar and equal to 0.998 for the long fibers mortar. Being r^2_{PRL} the highest among the regression coefficients, it implies that the parabolic function (described by $f_t(FC) = C_{FL}FC^2 + M_{FL}$) provides the best fitting for the experimental data (see Figure 12b). In the expression between parenthesis, C_{FL} and M_{FL} are regression constants peculiar to the specific fiber length. In particular, for the short fibers, the regression coefficients C_{12} and M_{12} are equal to 0.176 and 1.889 MPa, while for the long fibers, C_{24} and M_{24} are equal to 0.246 and 1.895 MPa, respectively. Hence, the equation for short fibers is $f_{t,F12} = 0.176FC^2 + 1.889$ and for long fibers $f_{t,F24} = 0.264FC^2 + 1.895$. As already previously noticed, the two regression coefficients M_{12} and M_{24} related to both fiber lengths are very similar and almost equal to the average tensile strength value $f_{t,0}$ of the unreinforced mortar samples (see Figure 8c). Based on this observation, we can assume M_{FL} to be length-independent and equal to the average tensile strength for unreinforced mortar samples; that is, $f_{t,0}$ = 1.9 MPa. On the other hand, the two angular coefficients C_{12} and C_{24} are respectively equal to 0.176 and 0.264 MPa, and they are fiber length dependent. In fact $C_{24} > C_{12}$, implying a greater tensile strength f_t of long fiber mortar samples for the entire range of variation of the FC. As already noticed for flexural strength and fracture energy, the results related to the tensile performance of the specimens strengthened with long fibers show a greater tensile strength f_t for all FC.

4.3. Compressive Behavior

The regression analysis of the compressive behavior is performed on the compressive strength f_c as a function of the fiber content and fiber length. Figure 12c shows the regression coefficient values r^2_{LRL}, r^2_{ERL}, and r^2_{PRL} for the linear, exponential, and parabolic regressions. r^2_{PRL} is the highest for both fiber lengths and equal to 0.997 and to 0.998 for the F24 and F12 case, respectively. Therefore the parabolic function, described by the generic form $f_c(FC) = D_{FL}FC^2 + N_{FL}$, provides the best fitting curves for the assigned data. The two equations for short and long fiber length mortars, obtained by replacing the specific regression coefficients D_{FL} and N_{FL} in the generic quadratic function, are depicted in Figure 12d. In particular, for the short fibers the regression coefficients D_{12} and N_{12} are equal to 1.5 and 17.5 MPa, respectively, while for long fibers D_{24} and N_{24} are equal to 2.0 and 17.5 MPa, respectively. Hence, the equation for the short fiber mortar is

$f_{c,F12} = 1.5FC^2 + 17.5$, while the equation for the long fiber mortar is $f_{c,F24} = 2.0FC^2 + 17.5$. As already noticed for the previous mechanical parameters, it is important to underline that N_{FL} is length independent, hence the two regression coefficients values N_{12} and N_{24} coincide; they are also equal to the average compressive strength value of the unreinforced mortar samples $f_{c,0}$ (depicted in Figure 8d). Moreover, by comparing the two angular coefficients D_{12} and D_{24}, depicted by red and orange dotted lines in Figure 12d and respectively equal to 1.5 and 2.0 MPa, D_{FL} results are greater for the fiber-strengthened mortar samples ($D_{24} > D_{12}$), implying a better compressive strength of long fiber mortars, although less marked respect to both the tensile and flexural behaviors.

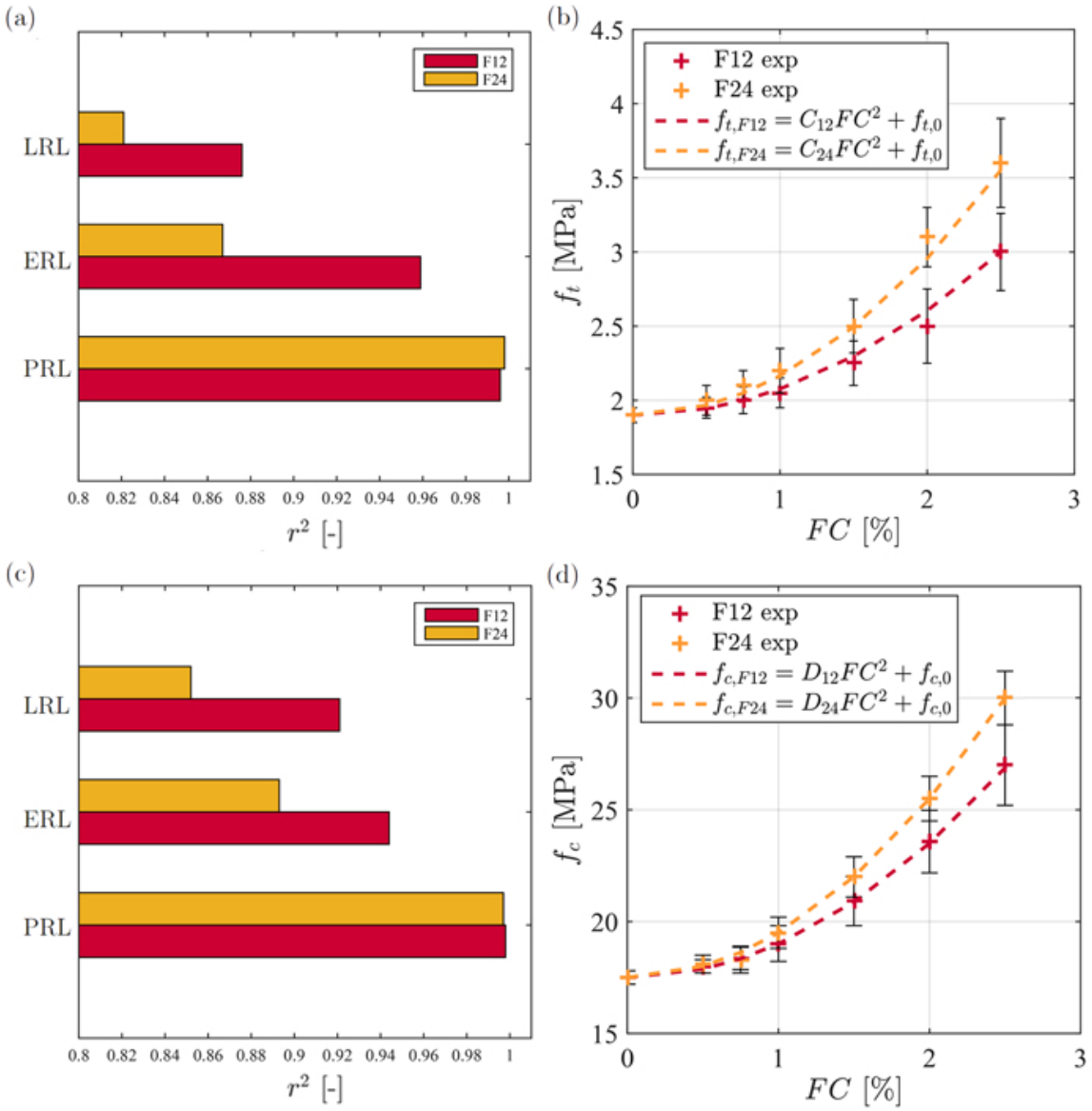

Figure 12. (**a**) Coefficients of determination r^2 for the tensile strength calculated for the linear (LRL), exponential (ERL), and parabolic (PRL) regression models, for both short and long basalt fibers; (**b**) tensile behavior regression lines as a function of the fiber content; (**c**) coefficients of determination r^2 for the compressive strength calculated with the three mentioned regression models, i.e., with LRL, ERL, and PRL; (**d**) compressive strength regression lines as a function of the fiber content.

5. Conclusions

This paper aims to characterize a sustainable material to be used for the restoration and strengthening of historical masonry structures: a lime-based mortar reinforced with

randomly oriented basalt fibers. More specifically, this study investigates the effect on the mortar's mechanical properties due to variation in the basalt fiber length (FL) and the basalt fiber content (FC).

The obtained results suggest drawing the following conclusions:

- The basalt fiber reinforced mortar shows a linear increase in its flexural strength while augmenting the content of fibers; this result is valid for both short length (SFL) and long length (LFL) basalt fibers. The flexural strength reaches an increase of 500% for SFL and 590% for LFL when compared to unreinforced prisms.
- The fracture energy linearly increases with increases in fiber content for both short and long fibers. If the fiber content is the maximum, the fracture energy enhances 600% for short fiber mortar and 1590% for long fiber mortar compared with unreinforced prisms.
- The tensile strength of the basalt prisms parabolically enhances while the content of fiber augments, and this increase is larger for high-length fibers than for low-length ones. In correspondence with the largest value of the content of fibers, the tensile strength grows 160% for SFL and 190% for LFL when compared with the unreinforced prisms.
- The basalt fiber reinforced mortar is characterized by a quadratic increase in its compressive strength while the content of fiber increases for both lengths of fiber. In correspondence with the largest value of the content of fibers, the compressive strength reaches an increase of 150% for SFL and 170% for LFL when compared with unreinforced prisms.
- The workability of the basalt-reinforced mortar is affected by both fiber length and fiber content; it always diminishes, as the content and length of fibers increases. As a consequence, considering a specific fiber content, the workability of the basalt conglomerate is always smaller for LFL prisms when compared with SFL ones.

The findings of this study are relevant in the field of civil engineering and architecture, as the newly developed mortar is suitable to be applied to large-scale retrofitting projects. The basalt fiber-enriched mortar stands as an innovative strengthening system that reduces both the costs and the application times when compared to traditional systems, as its workability is optimized to be applied to extensive surfaces.

Author Contributions: Conceptualization, M.M., M.V. and A.G.; methodology, M.M. and M.V.; software, M.M.; validation, M.V. and A.G.; formal analysis, M.M.; investigation, M.M.; data curation, M.M.; writing—original draft preparation, M.M.; writing—review and editing, M.M. and M.V.; visualization, M.M. and M.V.; supervision, A.G.; project administration, A.G.; funding acquisition, A.G. All authors have read and agreed to the published version of the manuscript.

Funding: The work of the first author was sponsored by the National Operational Programme on Research and Innovation 2014–2020 (CCI 2014IT16M2OP005) and the European Social Fund.

Data Availability Statement: Generated data will be made available on request.

Acknowledgments: Authors' acknowledgement goes to "Aquilaprem S.r.l." company (L'Aquila-Italy) for having provided the materials and the mix-design related to the plain mortar.

Conflicts of Interest: The authors declare no conflict of interest.

References

1. Asteris, P.G.; Chronopoulos, M.; Chrysostomou, C.; Varum, H.; Plevris, V.; Kyriakides, N.; Silva, V. Seismic vulnerability assessment of historical masonry structural systems. *Eng. Struct.* **2014**, *62*, 118–134. [CrossRef]
2. Ferreira, T.M.; Costa, A.A.; Costa, A. Analysis of the out-of-plane seismic behavior of unreinforced masonry: A literature review. *Int. J. Archit. Herit.* **2015**, *9*, 949–972. [CrossRef]

3. Chieffo, N.; Clementi, F.; Formisano, A.; Lenci, S. Comparative fragility methods for seismic assessment of masonry buildings located in Muccia (Italy). *J. Build. Eng.* **2019**, *25*, 100813. [CrossRef]
4. D'altri, A.M.; Sarhosis, V.; Milani, G.; Rots, J.; Cattari, S.; Lagomarsino, S.; Sacco, E.; Tralli, A.; Castellazzi, G.; De Miranda, S. Modeling strategies for the computational analysis of unreinforced masonry structures: Review and classification. *Arch. Comput. Methods Eng.* **2020**, *27*, 1153–1185. [CrossRef]
5. Lagomarsino, S.; Cattari, S.; Ottonelli, D. The heuristic vulnerability model: Fragility curves for masonry buildings. *Bull. Earthq. Eng.* **2021**, *19*, 3129–3163. [CrossRef]
6. Gregori, A.; Mercuri, M.; Angiolilli, M.; Pathirage, M. Simulating defects in brick masonry panels subjected to compressive loads. *Eng. Struct.* **2022**, *263*, 114333. [CrossRef]
7. Mercuri, M.; Pathirage, M.; Gregori, A.; Cusatis, G. Fracturing and collapse behavior of masonry vaulted structures: A lattice-discrete approach. *Procedia Struct. Integr.* **2023**, *44*, 1276–1283. [CrossRef]
8. Mercuri, M.; Pathirage, M.; Gregori, A.; Cusatis, G. Influence of self-weight on size effect of quasi-brittle materials: Generalized analytical formulation and application to the failure of irregular masonry arches. *Int. J. Fract.* **2024**, *246*, 117–144. [CrossRef]
9. Feilden, B.M.; Jokilehto, J. Management guidelines for world cultural heritage sites 1998. *Hist. Cities Issues Urban Conserv.* **2019**, *8*, 425.
10. ICOMOS. Recommendations for the Analysis, Conservation and Structural Restoration of Architectural Heritage. *Icomos International Scientific Committee for Analysis and Restoration of Structures of Architectural Heritage* 22/5/2003. Available online: https://ancientgeorgia.wordpress.com/wp-content/uploads/2012/04/recommendations_icomos-principles-and-guidelines.pdf (accessed on 3 January 2025).
11. *ISO 13822*; Bases for Design of Structures-Assessment of Existing Structures. CEN: Bruxelles, Brussels, 2005.
12. Brandi, C. *Teoria del Restauro*; Edizioni di Storia e Letteratura: Rome, Italy, 1963. Available online: https://www.amazon.it/Teoria-del-restauro-Cesare-Brandi/dp/8806155652 (accessed on 9 January 2025).
13. Maramotti, A.L. *La Materia del Restauro*; F. Angelli: Rome, Italy, 1990. Available online: https://www.francoangeli.it/Libro/La-materia-del-restauro?Id=1064 (accessed on 9 January 2025).
14. D'Ayala, D. Conservation principles and performance based strengthening of heritage buildings in post-event reconstruction. In *Perspectives on European Earthquake Engineering and Seismology*; Springer: Cham, Switzerland, 2014; pp. 489–514.
15. Vailati, M.; Gregori, A.; Mercuri, M.; Monti, G. A non-intrusive seismic retrofitting technique for masonry infills based on bed-joint sliding. *J. Build. Eng.* **2023**, *69*, 106208. [CrossRef]
16. Vailati, M.; Mercuri, M.; Gregori, A. Out-of-plane non-intrusive seismic retrofitting of in-plane damaged masonry infill through 3D printed recycled plastic devices. *Constr. Build. Mater.* **2024**, *438*, 137256. [CrossRef]
17. Gregori, A.; Castoro, C.; Mercuri, M.; Di Natale, A.; Di Giampaolo, E. Innovative Use of UHF-RFID Wireless Sensors for Monitoring Cultural Heritage Structures. *Buildings* **2024**, *14*, 1155. [CrossRef]
18. dei Ministri, P.D.C. *Valutazione e Riduzione del Rischio Sismico del Patrimonio Culturale con Riferimento alle Norme Tecniche per le Costruzioni di cui al decreto del Ministero delle Infrastrutture e dei Trasporti del 14 Gennaio 2008*; Direttiva PCM: Rome, Italy, 2011; Volume 9.
19. Gazzetta Ufficiale. Supplementary document: Official Supplementary Document No. 8. Available online: https://www.gazzettaufficiale.it/ (accessed on 9 January 2025).
20. Italian Ministry of Infrastructure and Transport (Ministero delle Infrastrutture e dei Trasporti). Available online: https://www.gazzettaufficiale.it/ (accessed on 9 January 2025).
21. Triantafillou, T.C. Strengthening of masonry structures using epoxy-bonded FRP laminates. *J. Compos. Constr.* **1998**, *2*, 96–104. [CrossRef]
22. Valluzzi, M.R.; Tinazzi, D.; Modena, C. Shear behavior of masonry panels strengthened by FRP laminates. *Constr. Build. Mater.* **2002**, *16*, 409–416. [CrossRef]
23. Tumialan, J.G.; Micelli, F.; Nanni, A. Strengthening of masonry structures with FRP composites. In *Structures 2001: A Structural Engineering Odyssey*; American Society of Civil Engineers: Reston, VA, USA, 2001; pp. 1–8.
24. Carloni, C.; Subramaniam, K.V. FRP-masonry debonding: Numerical and experimental study of the role of mortar joints. *J. Compos. Constr.* **2012**, *16*, 581–589. [CrossRef]
25. Foraboschi, P. Effectiveness of novel methods to increase the FRP-masonry bond capacity. *Compos. Part B Eng.* **2016**, *107*, 214–232. [CrossRef]
26. Grande, E.; Milani, G.; Sacco, E. Modelling and analysis of FRP-strengthened masonry panels. *Eng. Struct.* **2008**, *30*, 1842–1860. [CrossRef]
27. Marcari, G.; Manfredi, G.; Prota, A.; Pecce, M. In-plane shear performance of masonry panels strengthened with FRP. *Compos. Part B Eng.* **2007**, *38*, 887–901. [CrossRef]
28. Kišiček, T.; Stepinac, M.; Renić, T.; Hafner, I.; Lulić, L. Strengthening of masonry walls with FRP or TRM. *Građevinar* **2020**, *72*, 937–953.

29. D'Ambrisi, A.; Feo, L.; Focacci, F. Experimental and analytical investigation on bond between Carbon-FRCM materials and masonry. *Compos. Part B Eng.* **2013**, *46*, 15–20. [CrossRef]
30. Carozzi, F.G.; Milani, G.; Poggi, C. Mechanical properties and numerical modeling of Fabric Reinforced Cementitious Matrix (FRCM) systems for strengthening of masonry structures. *Compos. Struct.* **2014**, *107*, 711–725. [CrossRef]
31. Maddaloni, G.; Cascardi, A.; Balsamo, A.; Di Ludovico, M.; Micelli, F.; Aiello, M.A.; Prota, A. Confinement of full-scale masonry columns with FRCM systems. *Key Eng. Mater.* **2017**, *747*, 374–381. [CrossRef]
32. Bellini, A.; Incerti, A.; Bovo, M.; Mazzotti, C. Effectiveness of FRCM reinforcement applied to masonry walls subject to axial force and out-of-plane loads evaluated by experimental and numerical studies. *Int. J. Archit. Herit.* **2018**, *12*, 376–394. [CrossRef]
33. D'Ambra, C.; Lignola, G.P.; Prota, A. Simple method to evaluate FRCM strengthening effects on in-plane shear capacity of masonry walls. *Constr. Build. Mater.* **2021**, *268*, 121125. [CrossRef]
34. Ferretti, F.; Mazzotti, C. FRCM/SRG strengthened masonry in diagonal compression: Experimental results and analytical approach proposal. *Constr. Build. Mater.* **2021**, *283*, 122766. [CrossRef]
35. Castori, G.; Corradi, M.; Sperazini, E. Full size testing and detailed micro-modeling of the in-plane behavior of FRCM–reinforced masonry. *Constr. Build. Mater.* **2021**, *299*, 124276. [CrossRef]
36. Cucuzza, R.; Domaneschi, M.; Camata, G.; Marano, G.C.; Formisano, A.; Brigante, D. FRCM retrofitting techniques for masonry walls: A literature review and some laboratory tests. *Procedia Struct. Integr.* **2023**, *44*, 2190–2197. [CrossRef]
37. Rotunno, T.; Fagone, M.; Grande, E.; Milani, G. FRCM-to-masonry bonding behaviour in the case of curved surfaces: Experimental investigation. *Compos. Struct.* **2023**, *313*, 116913. [CrossRef]
38. Castellano, A.; Fraddosio, A.; Oliveira, D.V.; Piccioni, M.D.; Ricci, E.; Sacco, E. An effective numerical modelling strategy for FRCM strengthened curved masonry structures. *Eng. Struct.* **2023**, *274*, 115116. [CrossRef]
39. Napoli, A.; Realfonzo, R. Confinement of masonry with FRCM composites: Strength predictive models. *Compos. Struct.* **2024**, *331*, 117864. [CrossRef]
40. Ascione, L.; Feo, L.; Fraternali, F. Load carrying capacity of 2D FRP/strengthened masonry structures. *Compos. Part B Eng.* **2005**, *36*, 619–626. [CrossRef]
41. Valluzzi, M.R.; Valdemarca, M.; Modena, C. Behavior of brick masonry vaults strengthened by FRP laminates. *J. Compos. Constr.* **2001**, *5*, 163–169. [CrossRef]
42. Banijamali, S.M.; Esfahani, M.R.; Nosratollahi, S.; Sohrabi, M.R.; Mousavi, S.R. Reviewing the FRP strengthening systems. *Am. J. Civ. Eng.* **2015**, *3*, 38–43. [CrossRef]
43. Yun, Y.; Wu, Y.F.; Tang, W.C. Performance of FRP bonding systems under fatigue loading. *Eng. Struct.* **2008**, *30*, 3129–3140. [CrossRef]
44. Incerti, A.; Santandrea, M.; Carloni, C.; Mazzotti, C. Destructive in situ tests on masonry arches strengthened with FRCM composite materials. *Key Eng. Mater.* **2017**, *747*, 567–573. [CrossRef]
45. Padalu, P.; Singh, Y.; Das, S. Efficacy of basalt fibre reinforced cement mortar composite for out-of-plane strengthening of unreinforced masonry. *Constr. Build. Mater.* **2018**, *191*, 1172–1190. [CrossRef]
46. Faella, C.; Martinelli, E.; Nigro, E.; Paciello, S. Shear capacity of masonry walls externally strengthened by a cement-based composite material: An experimental campaign. *Constr. Build. Mater.* **2010**, *24*, 84–93. [CrossRef]
47. Alecci, V.; De Stefano, M.; Luciano, R.; Rovero, L.; Stipo, G. Experimental investigation on bond behavior of cement-matrix–based composites for strengthening of masonry structures. *J. Compos. Constr.* **2016**, *20*, 04015041. [CrossRef]
48. Deng, M.; Yang, S. Cyclic testing of unreinforced masonry walls retrofitted with engineered cementitious composites. *Constr. Build. Mater.* **2018**, *177*, 395–408. [CrossRef]
49. Briccoli Bati, S.; Rovero, L.; Tonietti, U. Strengthening masonry arches with composite materials. *J. Compos. Constr.* **2007**, *11*, 33–41. [CrossRef]
50. Chellapandian, M.; Prakash, S.S. Applications of Fabric Reinforced Cementitious Mortar (FRCM) in Structural Strengthening. In *Emerging Trends of Advanced Composite Materials in Structural Applications*; Springer: Berlin/Heidelberg, Germany, 2021; pp. 201–233.
51. Kal, K.W.; Lee, D.H.; Bang, Y.S.; Cho, H.C.; Kang, J.O.; Kim, K.S. The effectiveness of steel fibers as shear reinforcement. In *Proceedings of the Korea Concrete Institute Conference*; Korea Concrete Institute: Seoul, Republic of Korea, 2009; pp. 59–60.
52. Maage, M. Interaction between steel fibers and cement based matrixes. *Matériaux Constr.* **1977**, *10*, 297–301. [CrossRef]
53. Morgan, P. *Carbon Fibers and Their Composites*; CRC Press: Boca Raton, FL, USA, 2005.
54. Faleschini, F.; Zanini, M.A.; Hofer, L.; Pellegrino, C. Experimental behavior of reinforced concrete columns confined with carbon-FRCM composites. *Constr. Build. Mater.* **2020**, *243*, 118296. [CrossRef]
55. D'Antino, T.; Poggi, C. Stress redistribution in glass fibers of G-FRCM composites. *Key Eng. Mater.* **2019**, *817*, 520–527. [CrossRef]
56. Žmindák, M.; Dudinskỳ, M. Computational modelling of composite materials reinforced by glass fibers. *Procedia Eng.* **2012**, *48*, 701–710. [CrossRef]

57. Ochirbud, M.; Choi, D.; Naidanjav, U.; Ha, S.; Lee, C. Mechanical characterization of a FRCM system with aramid fiber fabric embedded in green high-strength cementitious matrix. *J. Asian Concr. Fed.* **2020**, *6*, 1–13. [CrossRef]
58. Caggegi, C.; Carozzi, F.G.; De Santis, S.; Fabbrocino, F.; Focacci, F.; Hojdys, Ł.; Lanoye, E.; Zuccarino, L. Experimental analysis on tensile and bond properties of PBO and aramid fabric reinforced cementitious matrix for strengthening masonry structures. *Compos. Part B Eng.* **2017**, *127*, 175–195. [CrossRef]
59. Mercuri, M.; Vailati, M.; Gregori, A. Lime-based mortar reinforced with randomly oriented polyvinyl-alcohol (PVA) fibers for strengthening historical masonry structures. *Dev. Built Environ.* **2023**, *14*, 100152. [CrossRef]
60. de Carvalho Bello, C.B.; Boem, I.; Cecchi, A.; Gattesco, N.; Oliveira, D.V. Experimental tests for the characterization of sisal fiber reinforced cementitious matrix for strengthening masonry structures. *Constr. Build. Mater.* **2019**, *219*, 44–55. [CrossRef]
61. Cristaldi, G.; Latteri, A.; Recca, G.; Cicala, G. Composites based on natural fibre fabrics. *Woven Fabr. Eng.* **2010**, *17*, 317–342.
62. Ticoalu, A.; Aravinthan, T.; Cardona, F. A review of current development in natural fiber composites for structural and infrastructure applications. In Proceedings of the Southern Region Engineering Conference (SREC 2010), Toowoomba, Australia, 10–12 November 2010; pp. 113–117.
63. Vailati, M.; Mercuri, M.; Angiolilli, M.; Gregori, A. Natural-fibrous lime-based mortar for the rapid retrofitting of heritage masonry buildings. *Fibers* **2021**, *9*, 68. [CrossRef]
64. Kouris, L.A.S.; Triantafillou, T.C. State-of-the-art on strengthening of masonry structures with textile reinforced mortar (TRM). *Constr. Build. Mater.* **2018**, *188*, 1221–1233. [CrossRef]
65. Rossi-Doria, P.R. Mortars for restoration: Basic requirements and quality control. *Mater. Constr.* **1986**, *19*, 445–448. [CrossRef]
66. Moropoulou, A.; Bakolas, A.; Bisbikou, K. Investigation of the technology of historic mortars. *J. Cult. Herit.* **2000**, *1*, 45–58. [CrossRef]
67. Moropoulou, A.; Cakmak, A.; Biscontin, G.; Bakolas, A.; Zendri, E. Advanced Byzantine cement based composites resisting earthquake stresses: The crushed brick/lime mortars of Justinian's Hagia Sophia. *Constr. Build. Mater.* **2002**, *16*, 543–552. [CrossRef]
68. Lanas, J.; Alvarez-Galindo, J.I. Masonry repair lime-based mortars: Factors affecting the mechanical behavior. *Cem. Concr. Res.* **2003**, *33*, 1867–1876. [CrossRef]
69. Lanas, J.; Bernal, J.P.; Bello, M.; Galindo, J.A. Mechanical properties of natural hydraulic lime-based mortars. *Cem. Concr. Res.* **2004**, *34*, 2191–2201. [CrossRef]
70. *Eurocode 6: Design of Masonry Structures—Part 1-1: General Rules for Reinforced and Unreinforced Masonry Structures.* Comité Européen de Normalisation: Brussels, Belgium, 2005.
71. Monaldo, E.; Nerilli, F.; Vairo, G. Basalt-based fiber-reinforced materials and structural applications in civil engineering. *Compos. Struct.* **2019**, *214*, 246–263. [CrossRef]
72. Dhand, V.; Mittal, G.; Rhee, K.Y.; Park, S.J.; Hui, D. A short review on basalt fiber reinforced polymer composites. *Compos. Part B Eng.* **2015**, *73*, 166–180. [CrossRef]
73. Khandelwal, S.; Rhee, K.Y. Recent advances in basalt-fiber-reinforced composites: Tailoring the fiber-matrix interface. *Compos. Part B Eng.* **2020**, *192*, 108011. [CrossRef]
74. Afroz, M.; Patnaikuni, I.; Venkatesan, S. Chemical durability and performance of modified basalt fiber in concrete medium. *Constr. Build. Mater.* **2017**, *154*, 191–203. [CrossRef]
75. Qin, J.; Qian, J.; Li, Z.; You, C.; Dai, X.; Yue, Y.; Fan, Y. Mechanical properties of basalt fiber reinforced magnesium phosphate cement composites. *Constr. Build. Mater.* **2018**, *188*, 946–955. [CrossRef]
76. Pehlivan, A.O. Investigation of fracture parameters of concrete incorporating basalt fibers. *Rev. Română De Mater. J. Mater.* **2021**, *51*, 247–255.
77. Wang, Y.; Kang, A.H.; Wu, Z.G.; Xiao, P.; Gong, Y.F.; Sun, H.F. Investigation of the basalt fiber type and content on performances of cement mortar and concrete. *Constr. Build. Mater.* **2023**, *408*, 133720. [CrossRef]
78. Li, Z.; Guo, T.; Chen, Y.; Fang, C.; Chang, Y.; Nie, J. Influence of basalt fiber and polypropylene fiber on the mechanical and durability properties of cement-based composite materials. *J. Build. Eng.* **2024**, *90*, 109335. [CrossRef]
79. Jiang, C.; Fan, K.; Wu, F.; Chen, D. Experimental study on the mechanical properties and microstructure of chopped basalt fibre reinforced concrete. *Mater. Des.* **2014**, *58*, 187–193. [CrossRef]
80. Wang, X.; He, J.; Mosallam, A.S.; Li, C.; Xin, H. The effects of fiber length and volume on material properties and crack resistance of basalt fiber reinforced concrete (BFRC). *Adv. Mater. Sci. Eng.* **2019**, *2019*, 7520549. [CrossRef]
81. High, C.; Seliem, H.M.; El-Safty, A.; Rizkalla, S.H. Use of basalt fibers for concrete structures. *Constr. Build. Mater.* **2015**, *96*, 37–46. [CrossRef]
82. Elshafie, S.; Whittleston, G. A review of the effect of basalt fibre lengths and proportions on the mechanical properties of concrete. *Int. J. Res. Eng. Technol.* **2015**, *4*, 458–465.
83. Ralegaonkar, R.; Gavali, H.; Aswath, P.; Abolmaali, S. Application of chopped basalt fibers in reinforced mortar: A review. *Constr. Build. Mater.* **2018**, *164*, 589–602. [CrossRef]

84. Jiang, C.H.; McCarthy, T.J.; Chen, D.; Dong, Q. Influence of basalt fiber on performance of cement mortar. *Key Eng. Mater.* **2010**, *426*, 93–96. [CrossRef]
85. Chen, H.; Xie, C.; Fu, C.; Liu, J.; Wei, X.; Wu, D. Orthogonal Analysis on Mechanical Properties of Basalt–Polypropylene Fiber Mortar. *Materials* **2020**, *13*, 2937. [CrossRef] [PubMed]
86. Arandigoyen, M.; Alvarez, J. Pore structure and mechanical properties of cement–lime mortars. *Cem. Concr. Res.* **2007**, *37*, 767–775. [CrossRef]
87. *UNI EN 1015-11: 2019*; Methods of Test for Mortar for Masonry—Part 11: Determination of Flexural and Compressive Strength of Hardened Mortar. UNI—Ente Italiano di Normazione: Milano, Italy, 2019.
88. *ASTM C1437-07*; Standard Test Method for Flow of Hydraulic Cement Mortar. Annual Book of ASTM Standards. ASTM: West Conshohocken, PA, USA, 2007.
89. RILEM Technical Committee. Determination of the fracture energy of mortar and concrete by means of three-point bend tests on notched beams. *Mater. Struct.* **1985**, *18*, 285–290. [CrossRef]
90. Shah, S.P. Size-effect method for determining fracture energy and process zone size of concrete. *Mater. Struct.* **1990**, *23*, 461–465. [CrossRef]
91. Bažant, Z.P. *Fracture and Size Effect in Concrete and Other Quasibrittle materials*; Routledge: London, UK, 2019.
92. Griffith, A.A. VI. The phenomena of rupture and flow in solids. *Philos. Trans. R. Soc. Lond. Ser. A Contain. Pap. A Math. Phys. Character* **1921**, *221*, 163–198.
93. Bakeer, T. *Collapse Analysis of Masonry Structures Under Earthquake Actions*; Lehrstuhl Tragwerksplanung: Dresden, Germany, 2009; Volume 8. Available online: https://www.academia.edu/47724637/Collapse_Analysis_of_Masonry_Structures_under_Earthquake_Actions (accessed on 9 January 2025).
94. Vailati, M.; Mercuri, M.; Gregori, A. One-head masonry panels reinforced with industrial-waste fiber reinforced mortar: Investigating the effect of bed joints and coating reinforcement in the diagonal compressive behavior. *Structures* **2024**, *63*, 106474. [CrossRef]
95. Mercuri, M.; Vailati, M.; Gregori, A. Two-heads brick masonry walls strengthened by basalt and glass chopped fiber mortar: Effect of bed joints and coating reinforcements. *Structures* **2024**, *64*, 106530. [CrossRef]
96. Mercuri, M.; Pathirage, M.; Gregori, A.; Cusatis, G. Computational modeling of the out-of-plane behavior of unreinforced irregular masonry. *Eng. Struct.* **2020**, *223*, 111181. [CrossRef]
97. Mercuri, M.; Pathirage, M.; Gregori, A.; Cusatis, G. On the collapse of the masonry Medici tower: An integrated discrete-analytical approach. *Eng. Struct.* **2021**, *246*, 113046. [CrossRef]
98. Mercuri, M.; Pathirage, M.; Gregori, A.; Cusatis, G. Masonry vaulted structures under spreading supports: Analyses of fracturing behavior and size effect. *J. Build. Eng.* **2022**, *45*, 103396. [CrossRef]
99. Fox, J. *Applied Regression Analysis and Generalized Linear Models*; Sage Publications: Thousand Oaks, CA, USA, 2015.
100. Duchesne, P.; Rémillard, B. *Statistical Modeling and Analysis for Complex Data Problems*; Springer Science & Business Media: Berlin, Germany, 2005; Volume 1.